

ABSTRACT

Title of Thesis: INVESTIGATION OF SUPERSONIC MIXING USING
LASER-INDUCED BREAKDOWN SPECTROSCOPY

Degree Candidate: Travis Tempel

Degree and year: Master of Science, 2004

Thesis directed by: Assistant Professor Steven G. Buckley
Department of Mechanical Engineering

Supersonic mixing enhancement techniques are of considerable interest; typically qualitative observations of shear layer growth rate are used to compare these techniques. A more accurate assessment of the efficiency of various mixing techniques could be made using local species concentrations at specific points. Laser-induced breakdown spectroscopy (LIBS), which can determine local elemental concentrations in a flowfield, is applied to the supersonic mixing problem in this work.

An investigation of mixing caused by cavity-induced resonance was completed in a Mach 2 wind tunnel using LIBS. Calibration experiments showed that LIBS is capable of measuring helium concentrations with $\pm 5\%$, $\pm 15\%$, $\pm 25\%$, and $\pm 40\%$ fractional error for ranges of 0-25%, 25-45%, 45-75%, and 75-100% helium. Quantitative helium concentration measurements were performed at several points in the flow field. The results showed that cavity-induced resonance caused an increase in the mixing between helium and air in supersonic flow.

INVESTIGATION OF SUPERSONIC MIXING USING LASER-INDUCED
BREAKDOWN SPECTROSCOPY

By

Travis Tempel

Thesis submitted to the Faculty of the Graduate School of the
University of Maryland, College Park in partial fulfillment
of the requirements for the degree of
Master of Science
2004

Advisory Committee

Assistant Professor Steven G. Buckley, Chair/Advisor
Associate Professor Kenneth Yu
Associate Professor Kenneth Kiger

© Copyright by

Travis Tempel

2004

ACKNOWLEDGEMENTS

I would like to thank my advisor, Dr. Steven Buckley, for his support throughout my entire graduate school career. He has provided invaluable assistance and advice during the past two years and without him this would not be possible. I would like to thank Dr. Kenneth Yu for his support and generosity with his laboratory and his time and I would like to thank Dr. Kenneth Kiger for volunteering to sit on my thesis committee.

The Mechanical Engineering graduate office and various members of the faculty and staff of the department deserve my thanks as well. Without their efforts and constant reminders, this research could not have gone as well as it did.

This thesis is dedicated to both my friends and family that have supported me in more ways than I can count. This goes especially for my mother, who was able to teach her children to value education above all other things.

TABLE OF CONTENTS

ABSTRACT	i
ACKNOWLEDGEMENTS.....	ii
TABLE OF CONTENTS.....	iii
LIST OF FIGURES	v
LIST OF TABLES	viii
TABLE OF NOMENCLATURE	ix
CHAPTER 1 Introduction.....	1
1.1 Background	1
1.2 Laser-Induced Breakdown Spectroscopy (LIBS).....	2
1.3 Supersonic mixing	4
1.4 Objectives	7
CHAPTER 2 Literature Review.....	8
2.1 Laser-Induced Breakdown Spectroscopy	8
2.2 Cavity-actuated Supersonic Mixing	12
CHAPTER 3 Apparatus and Calibration	15
3.1 Calibration	15
3.2 LIBS Setup	15
3.3 Initial Calibration	20
3.4 Annular Tubes – Diffusion Experiment	28
3.5 Fluent Simulation	32
3.6 Theoretical Normalization.....	34
3.7 Calibration Data Summary.....	36

CHAPTER 4	Experimental Wind Tunnel Results	38
4.1	Experiments.....	38
4.2	Calibration	40
4.3	Experimental Results.....	42
4.4	Summary of Data.....	53
CHAPTER 5	Error Analysis	54
5.1	Sources of Error.....	54
5.2	Calculating Signal Intensity	58
CHAPTER 6	Conclusions.....	62
References	64
Appendix A	– Graphs from Coaxial Jet Experiment	69
Appendix B	– Graphs from Wind Tunnel Experiments	71
I	Baseline – No Cavity.....	71
II	With Cavity	72
Appendix C	– Matlab m-files	74
I	Signal Characterization	74
II	Annular Tube Experiment	75
III	Wind Tunnel Experiments.....	76
IV	Characteristic Line Calculation	78
V	Annular Tube Comparison	79
VI	Wind Tunnel Comparisons.....	80

LIST OF FIGURES

Figure 1 – Schlieren images of fuel-injection with and without a cavity from [20].	6
Figure 2 – LIBS data collection setup.	17
Figure 3 – Example spectra when measuring helium intensity at 588 nm.	19
Figure 4 – Example spectra when measuring oxygen and nitrogen.	19
Figure 5 – Helium peak-to-base intensity at the four main wavelengths.	21
Figure 6 – Peak-to-base intensity of helium at 588 nm with error bars.	21
Figure 7 – Helium peak-to-base values at 588 nm.	23
Figure 8 – Oxygen and nitrogen peak-to-base intensity as a function of % helium.	23
Figure 9 – O / He ratio from three different experiments.	25
Figure 10 – Normalized residual between the three characterization experiments and the data fit.	26
Figure 11 – Fractional error at four different concentration ranges.	27
Figure 12 – Data fit curve with the total error in each concentration range with the experimental values.	28
Figure 13 – Spark locations during annular tube experiment.	29
Figure 14 -- Oxygen / helium ratio at various axial distances.	30
Figure 15 – Volumetric helium percentages at several axial distances.	31
Figure 16 – Mass fraction of H ₂ at various axial heights, obtained from FLUENT simulation.	33
Figure 17 – Experimental results compared with CFD results from FLUENT.	34
Figure 18 – Normalized mass fraction data obtained from FLUENT.	35
Figure 19 -- Normalized helium concentration curves obtained through experiments.	36
Figure 20 – Wind tunnel setup with close up of cavity test section.	39

Figure 21 – Placement of measurement points during wind tunnel experiments.	40
Figure 22 – Helium peak-to-base ratio with air at 20 psi and helium at 40 psi and 60 psi.	42
Figure 23 -- He / O intensity ratio at three downstream locations (w/o cavity).	43
Figure 24 – Single-shot values of He and O intensity at y = 0 and x = 6.3, 31.7, and 57.1 mm for the He/Air 60/20 pressure case (w/o cavity).	44
Figure 25 – Histograms of helium and oxygen intensity at y = 0 and x = 6.3, 31.7, and 57.1 mm for the He/Air 60/20 pressure case (w/o cavity).	45
Figure 26 – He / O intensity ratio at the three downstream locations for the He/Air 60/20 case (w/cavity).	46
Figure 27 – Single-shot values of He and O intensities at y = 0 and x = 6.3, 31.7, and 57.1 mm for the He/Air 60/20 pressure case (w cavity).	47
Figure 28 --Histograms of helium and oxygen intensity at y = 0 and x = 6.3, 31.7, and 57.1 mm for the He/Air 60/20 pressure case (w/cavity).	48
Figure 29 – Percent helium at the three downstream locations for the He/Air 60/20 pressure case (w/o cavity).	50
Figure 30 – Percent helium at the three downstream locations for the He/Air 60/20 pressure case (w/cavity).	51
Figure 31 – He / O intensity at x=6.3 mm downstream for He/Air 60/40 psi.	52
Figure 32 – He / O intensity at x=57.1 mm downstream for He/Air 60/40 psi.	52
Figure 33 – Oxygen intensities measured during wind tunnel testing at downstream (X) locations.	58
Figure 34 – He / O Ratio at various heights from February 2 nd	69

Figure 35 – He / O Ratio at various heights from February 3 rd	69
Figure 36 – He / O Ratio at various heights from February 3 rd (b).	70
Figure 37 – He / O Ratio at each point for the Air/He 20/40 psi case without the cavity. 71	
Figure 38 – He / O Ratio at each point for the Air/He 20/60 psi case without the cavity. 71	
Figure 39 – He / O Ratio at each point for the Air/He 40/60 psi case without the cavity. 72	
Figure 40 – He / O Ratio at each point for the Air/He 20/40 psi case with the cavity.	72
Figure 41 – He / O Ratio at each point for the Air/He 20/60 psi case with the cavity.	73
Figure 42 – He / O Ratio at each point for the Air/He 40/60 psi case with the cavity.	73

LIST OF TABLES

Table 1 – Calculated helium concentrations with error for the points shown in Figure 27.	50
Table 2 – Calculated helium concentrations with error for the points shown in Figure 28.	51
Table 3 – Fractional error in oxygen and helium intensity using PB and SNR during data fit experiment.	59
Table 4 – Values of total fractional error when using PB and SNR methods (40/20 case w/o cavity).....	60
Table 5 – Values of total fractional error when using PB and SNR methods (60/20 case w/o cavity).....	60
Table 6 – Values of total fractional error when using PB and SNR methods (60/40 case w/o cavity).....	60
Table 7 – Values of total fractional error when using PB and SNR methods (40/20 case with cavity).	61
Table 8 – Values of total fractional error when using PB and SNR methods (60/20 case with cavity).	61
Table 9 – Values of total fractional error when using PB and SNR methods (60/40 case with cavity).	61

TABLE OF NOMENCLATURE

FE	Fractional error
N_j	Number of data values in each range
R_N	Normalized residual
TE_i	Total error at each point
FE_j	Fractional error in each range
X_{data}	Experimental data value
X_{fit}	Data fit value
X_{mean}	Average intensity value
$\delta_{flowmeter}$	Error in flowmeter measurement

CHAPTER 1 INTRODUCTION

1.1 Background

Laser induced breakdown spectroscopy is a promising method for measuring local fuel/air ratios and quantitatively comparing supersonic mixing techniques. At supersonic speeds, a combustor is required to mix fuel and air with greater efficiency than at subsonic speeds due to a reduction in mixing length and decreasing residence time in combustion. Yet as flow compressibility increases, natural turbulent fluctuations are damped and mixing rates are decreased (Gutmark [15]). As discussed below, numerous mixing enhancement techniques have been developed for supersonic combustion and accurate measurement methods are needed to perform comparisons between these techniques.

Several well-established methods can be used for measuring fluid properties: strain gauges for measuring forces, pressure transducers for wall pressure, pitot tubes for stream velocity, temperature-sensitive paint for heat flux, thermocouples for temperature, etc. All of these methods are limited to points where the flow comes in contact with a wall or a nozzle. Because these devices require direct contact, they can cause great disturbances within the flow. To more accurately determine fluid properties, non-intrusive measurement methods are needed.

Generally, finding non-intrusive measurement methods is an important step in high speed flow research (Bonnet [1]). Laser diagnostic techniques are an attractive option requiring only optical access to the flow. This introduction provides a review of recent laser-induced breakdown spectroscopy experiments along with a comparison of other laser diagnostic methods for supersonic flow. Laser-induced breakdown spectroscopy

has not been used for measurements in a supersonic environment and the results in this thesis represent data that is the first of its kind.

1.2 Laser-Induced Breakdown Spectroscopy (LIBS)

LIBS uses a high-power, pulsed laser beam, focused onto a small point using a converging lens, to create a high-temperature plasma. The plasma fragments molecules into their constituent elements and excites electrons to super-equilibrium high energy states. When the electrons relax back to their ground state as the plasma cools, light is emitted at wavelengths unique to each element. The light is collected through a fiber-optic cable and sent to a spectrometer which disperses the light and records the intensity at each wavelength. Using the intensity of the atomic line emission, elemental concentrations and ratios can be found. The total size of the laser-induced plasma is 0.1-1 mm in diameter, depending on the laser pulse energy (Ferioli [7]), and the measurement is completed in microseconds, providing rapid, in-situ analysis of the flow.

LIBS is frequently used to analyze gas and particle composition. At Los Alamos, experiments were done to determine the presence of toxic gases or vapors in air and for measuring beryllium particles in air or on filters (Radziemski [8]). LIBS has been used for numerous types of analyses, including waste emission analysis, sorting material into correct scrap bins, and other material processing ([8], [26], [28]). The technique only requires visible access to the sample, and is non-invasive. Portable LIBS instruments have been developed in recent years (Song [17]), allowing measurements in a variety of non-laboratory environments.

There are many optically-based laser measurement techniques but according to Bonnet, et al. [1] the four most promising for supersonic flow are: laser induced

breakdown spectroscopy, Rayleigh scattering, Raman scattering, and coherent anti-Stokes Raman scattering. As discussed above, laser-induced breakdown spectroscopy (LIBS) can determine elemental concentrations at specific points in the flow, but is an emerging technology that it is not completely established. Although frequently used for the analysis of solids or waste processing, this laser diagnostic technique could be applied to supersonic flow.

Rayleigh scattering is the elastic scattering of light that occurs when electric fields of radiation interact with electric fields of molecules (Zhao [24]). The amount of scattered light increases with the density of the flow being sampled and it has the strongest signal of the molecular scattering techniques. Rayleigh scattering is proportional to the total density of the flow and is not species specific, so specific molar concentrations can only be determined in binary mixtures. If the species are known, the flow temperature can also be determined from the density.

Rayleigh scattering measurements are very sensitive to background sources of scattered light, since the signal is unshifted in wavelength from the laser, and the experiment must be optically isolated from any surface that could reflect the laser pulse. Rayleigh scattering is also limited to non-reacting flow, since the variation in density between the reactants, products, and intermediaries of the combustion process greatly affects the scattering cross section [24]. Measurements require a virtually particulate free environment. Only particles that have a diameter less than one-tenth of the incident light wavelength can be measured accurately. The scattering caused by particles larger than this is referred to as Mie scattering. Mie scattering generally involves seeding the flow with particles of a certain size and has been used previously for supersonic measurements

(Yu [11]). Rayleigh scattering can be applied to supersonic flow and experiments are planned in the near future.

Raman scattering is essentially the complement of Rayleigh scattering in that it is the inelastic light scattering from the interaction of the electric fields of radiation and molecules. Although much weaker than Rayleigh scattering, Raman signals are at wavelengths shifted from the laser wavelength and are thus insensitive to background sources of scattered laser light. Raman signals can be used to determine specific molecular concentrations because the wavelength shift depends on the species present [24]. These signals are extremely weak and difficult to detect, and past supersonic flow experiments have shown they are limited by measurement sensitivity [1].

Coherent anti-Stokes Raman scattering (CARS) uses two pump beams and one Stokes beam phase-matched to create a laser-like beam at a separate frequency. When this beam is close to a Raman transition frequency, the induced laser beam (CARS signal) is resonantly enhanced (Yang [21]). This method can determine the fluid velocity, temperature, density, and species concentration which could enhance further supersonic flow studies [21]. The CARS setup can include up to four different lasers and requires a complex alignment procedure, hindering both portability and practicality, and the investment required for lasers may be prohibitive [25]. The lower detection limits for O_2 and H_2 are also significantly higher than with LIBS [1].

1.3 Supersonic mixing

Mixing can be defined as a transport of properties between two dissimilar fluids (Nenmeni [29]). Momentum, species, and temperature are all examples of properties that

are commonly transported through mixing. For combustion to occur, fuel and air must be mixed at a molecular level. The region where this happens is referred to as the “mixing layer” or the “shear layer.” The second term is used because shear forces are most often responsible for much of the mixing.

The mixing layer can be defined as a region where there is a gradient between fluid properties. These gradients can cause instabilities, or turbulence, within the shear layer. Instabilities can cause large, coherent structures, or vortices, to form which increase the shear layer size and greatly enhance the mixing rate. Shear layer growth rate (δ/x) is one indicator of the overall level of mixing achieved in a flow. Many experiments have been done to determine the manner in which velocity and density changes affect the shear layer growth (Brown [30], Papamouschou [31]). The results relevant to this research show that an increase in Mach number causes a drastic reduction in shear layer growth rate.

At Mach 2.0, the shear layer growth rate can be reduced to almost 20% of its normal value (Seiner [32]). A lower shear layer growth rate reduces the amount of natural turbulent mixing between air and fuel in the intake and creates the need for a longer intake or mixing enhancement. A longer engine intake would increase the overall weight and size of a supersonic vehicle, two factors that are important to minimize. It is therefore advantageous to consider mixing enhancement methods in the design of any supersonic vehicle.

Methods that have been studied to enhance supersonic mixing and combustion include varying the number and orientation of fuel-injection ports and geometrically modifying the intake walls with ramps or cavities [15]. Most research focuses on

creating large scale coherent structures or vortices in the shear-layer although some experiments have found success in other areas such as reducing jet noise or thrust vector control. Both passive and active control methods may enhance mixing. Passive control uses only geometrical modifications to enhance shear layer growth in the flow. Active control methods use external forcing to mechanically alter the flow such as fluctuating flaps, periodic suction or blowing, or acoustic excitation.

Passive control of supersonic mixing using wall cavities is a promising technique. An open rectangular, or semi-circular, cavity mounted adjacent to the jet exit plane causes pressure oscillations that form large coherent structures. The cavity sheds these structures from its trailing edge at a resonant frequency based on the length/depth ratio of the cavity [20]. The structures increase the shear layer growth rate and increase the amount of fuel and air mixing in the compressible flow. Previous experiments have shown up to a 3-fold increase in the spreading rate of initial shear layers due to flow-induced cavity resonance (Yu [11]). The change in flow behavior due to a wall cavity in Mach 2.0 airflow can be seen in Figure 1 from Burnes, Parr, and Yu [20].

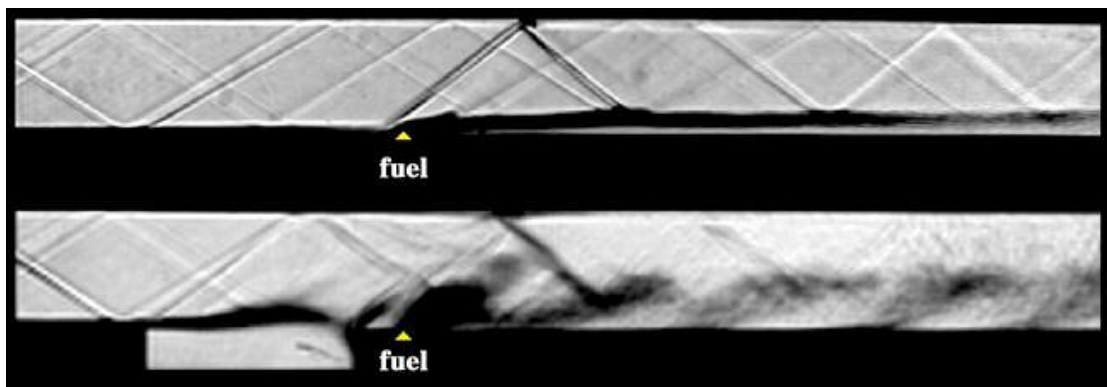


Figure 1 – Schlieren images of fuel-injection with and without a cavity from [20].

Experiments with cavity-actuated supersonic mixing have relied on phase-lock Schlieren imaging and Mie scattering images for visualization of the shear layer growth rates [11]. These tests proved qualitatively that cavity-actuated supersonic mixing could enhance the shear layer growth rate, but did not provide information on local fuel/air ratios to quantify the improvement in mixing. While a direct correlation between shear layer growth rate and flow mixing exists [15], the relationship between the two is not specifically defined and a better means of quantifying the mixing enhancement would be beneficial.

1.4 Objectives

Detailed measurements are essential to understanding the effect that mixing enhancement techniques have on supersonic flow. The main focus of this thesis is to show that LIBS can be used in supersonic conditions to measure the air/fuel ratio at specific points in the flowfield. Tests are accomplished using both a baseline case and a wall cavity at various air and fuel pressures to illustrate the use of LIBS in high speed shear flows.

CHAPTER 2 LITERATURE REVIEW

2.1 Laser-Induced Breakdown Spectroscopy

LIBS has been used for measuring atomic concentrations in gas, liquid, and solid samples [36], [37]. The LIBS microplasma measures local elemental concentrations before, after, and even during combustion without the need to seed the flow. The high intensity electric field of the focal point of the laser strips outer-shell electrons from molecules in the sample volume. This inverse bremsstrahlung increases the optical thickness of the focal volume, promoting further optical absorption that creates a microplasma. The plasma initially reaches a temperature well over 20,000K (Rusak [23]), hence regardless of the initial sample temperature or state, all molecules are broken down into their constituent elements. Within approximately one microsecond after plasma initiation, local thermodynamic equilibrium is reached and subsequently, atomic emission measurements can be performed. LIBS is currently used for waste emission analysis, environmental monitoring, and various material processing (Sneddon [26]). There has been no literature regarding LIBS being used in a supersonic environment or to measure specific helium concentrations.

Hahn and co-workers used LIBS as an in-situ, noninvasive, continuous emissions monitor for metals in waste streams (Hahn et al.[3], Buckley et al.[5]). Metal particulates in effluent streams can undergo numerous reactions and condense on preexisting particles or nucleate new particles. Most metals present in hazardous waste streams condense on a specific site and are either embedded in particles or liquid aerosols [3]. LIBS has the ability to measure these metals in process exhausts since the plasma is energetic enough

to completely disassociate particulate matter smaller than a few microns regardless of its initial state [35].

Studies have been performed to analyze metal particles, including efforts to compare LIBS analysis with the EPA Multi-Metals Sampling Train, known as EPA Method 29 (Buckley et al. [5]). The authors found lower sensitivity bounds for a number of elements using LIBS. Five out of six Resource and Recovery Act (RCRA) metals, Be, Cd, Cr, Hg, and Pb, had detection limits that met proposed Maximum Available Control Technology (MACT) standards. Additional tests were performed measuring Pb emission from the destruction of a Shillelagh rocket owned by the U.S. government.

Dudragne, et al. [22] performed calibration experiments for fluorine, chlorine, and sulfur to aid in the detection of hazardous gases or chemical weapons. Using time-resolved LIBS, the system was sensitive enough to measure 20 ppm fluorine, 90 ppm chlorine, and 1500 ppm of sulfur. LIBS was chosen because the method could be automated and could be extended to measure surfaces and liquids with only optical components, avoiding contamination. The experiment also proved that even very stable molecules such as SF₆ and CF₄ are completely broken down in the plasma.

LIBS has been used to measure equivalence ratios in the exhaust stream of an automobile engine (Ferioli [7]). Conventional oxygen sensors used as exhaust monitors are limited to a 50 ms response time which can not measure cycle-to-cycle air-fuel ratio. LIBS is only limited by the pulse speed of the laser and spectrometer collection limit. Measurements can be taken in as little as 20 μs, allowing phase-locked measurements to be taken at a specific engine cycle timing to provide cycle-resolved air-fuel ratios. The authors were able to determine the relative strength of C, O, N and CN emission lines and

determine the engine equivalence ratio from the ratio of emission lines. Results showed an almost linear relationship between the C/O, C/N, and air/fuel ratios.

Phouc, et al. [28] performed a study using the laser plasma as an ignition source. Laser plasmas are non-intrusive, requiring no anode or cathode, and are capable of providing sequential or simultaneous ignition at multiple sites. The laser emission and absorption characteristics of the ignition cell windows were studied in air, O₂, N₂, H₂, and CH₄. The absorption of the window was found to be between 5-10% of the laser energy. The authors also showed the spectrally broadband background emission was significant during the initial stages of spark development. During plasma cooling, line radiation dominated the emission. The oxygen peak could clearly be observed at 777 nm and the nitrogen peak could be observed at 746 nm.

There have been very few LIBS experiments dealing with helium. Hanafi, et al. [2] studied the effect of pressure change on helium emission intensity. The results showed that, in pure helium, the signal intensity increased as the helium pressure was increased up to 900 mbar, after which the intensity leveled off. From their results it is also possible to see that the strongest atomic emission line of helium is at 587.6 nm.

Detalle, et al. [10] used LIBS to analyze aluminum alloy samples with both air and helium as the surrounding gas. The authors stressed the importance of keeping the key parameters such as laser wavelength, pulse energy and duration, and the focusing conditions constant. The aluminum alloy sample was mounted to an XYZ stepping motor and either compressed air or helium was blown across the surface of the material during laser pulses. The results showed that helium produced a hotter spark that decayed faster than in air, which was attributed to helium having a higher thermal conductivity

than air at room temperature. Helium also yielded a lower electron density in air for the same pulse energy, which was attributed to the higher ionization potential of helium. The authors found that using helium as a buffer gas reduces the background emission and improves the signal-to-noise ratio.

Several methods have been used to process the spectral data obtained from LIBS experiments. There are two main ways to collect data: single-shot spectra giving a reading for each laser pulse, or ensemble-averaged spectra which combine multiple pulse measurements into one. Both have advantages depending on the circumstances in which measurements are taken.

Single-shot spectra allow analysis at a specific instant in time. This is the preferred measurement method for turbulent flows, since the elemental concentration at a specific point can fluctuate significantly. It is used when measurements can not be easily repeated, such as measuring unburned propane in air near $\Phi = 1$ when a spark could ignite the sample or for measurements of a dilute particle. Single-shot spectra can also be used for laminar cases when several rapid laser pulses could skew results by creating turbulence in the flowfield.

There are advantages to ensemble-averaged spectra measurements as well. Taking the average of multiple measurements helps to damp out any shot-to-shot fluctuations in laser power or other random noise. Averaging random events decreases background noise by $N^{-1/2}$, where N is the total number of shots. It was observed during the present experiments that time-averaged spectra taken at 10 Hz reduced the level of background noise, as reported in Chapter 5. Ensemble-averaged measurements are used when the intensity fluctuations are unimportant, such as when measuring a uniform gas.

The primary information obtained from LIBS spectra in these experiments is the elemental line intensity. There are two widely accepted methods to interpret the elemental line intensity, the peak-to-base ratio and the signal-to-noise ratio. The peak-to-base ratio is the integrated atomic line intensity divided by the average intensity of an adjacent, featureless emission range called the “baseline.” Since the baseline captures some continuum emission, the peak-to-base ratio minimizes the effect of fluctuations in laser power or signal due to absorption. The signal-to-noise ratio is defined as the integrated atomic line intensity divided by the rms noise. The rms noise was calculated as the deviation from a least-squares approximation of the same adjacent, featureless emission range used above to calculate the baseline. Carranza, et al. [9] performed both methods when calculating silicon emission intensity at 288.1 nm and determined that the signal-to-noise ratio provided a more robust metric for determining analyte detection from single-shot measurements of aerosol particles.

2.2 Cavity-actuated Supersonic Mixing

The focus of these experiments was on cavity-actuated supersonic mixing because of the readily-available setup and abundance of data from previous testing. Cavity actuated supersonic mixing involves placing an open trench, rectangular or semi-circular, adjacent to the jet entrance. Cavities cause large, coherent structures to form from pressure fluctuations at their resonant frequency. The cavities were originally used only for vortex manipulation and generation in the shear layer [11], but more recently they have been used as pilot flame holders to increase combustion efficiency [13]. A variety of techniques have been used to quantify and define the actual effect that vortices and flame holders have on the flow.

In the first experiments, with non-reacting jets, mixing was measured using a Mie scattering technique. The flow was seeded with 0.3 μm aluminum oxide particles which reflected light from a copper vapor laser beam. The beam was shaped into a thin sheet normal to the center axis of the jet and a CCD camera was used to capture the light emission. Time-averaged intensity profiles were obtained with the shear layer thickness defined as the distance between the 10% and 90% free stream intensity levels. Results showed up to a threefold increase in the shear layer growth rate between cold supersonic jets and a 50% increase in hot supersonic jets [11].

To measure reacting jets, a fuel-rich mixture was used, which caused an afterburning effect. The flames were recorded on super-VHS tape for analysis and several parameters including flame luminosity and distance from the jet exit were measured. Results showed that the afterburning intensity increased when the cavity resonance frequency was equal to or greater than the preferred mode frequency of the supersonic flow [12]. A more intense afterburn represents better mixing in the upstream flow.

Further experiments utilized cavities not only to enhance mixing, but for flame holding as well. A stable pilot flame located in a wall cavity results in a lower pressure drop than a bluff body flame holder and allows stable combustion at low equivalence ratios [13]. There was a significant increase in both the combustor pressure and exit recovery temperature when a cavity flame holder was used. The total pressure profile became more uniform in the cavity cases as well, indicating an increased level of mixing. The results showed that combustion is more efficient and mixing is increased when a cavity flame holder is used.

The next step was to investigate the effect that the fuel injection location would have on flow characteristics. A supersonic wind tunnel was built with visual access to the flow a priority [14]. A similar wind tunnel was used in the current LIBS experiments. Spark Schlieren images were taken through the side windows of the test cell for visualization. The effect that different fuels and fuel injection locations have on the large coherent structures downstream of the cavity was determined from these images. Results showed that fuel injected directly into the cavity suppresses the formation of coherent structures but forms a stable pilot flame. Fuel injected into the cavity wake, however, is entrained in the flow faster and leads to a higher level of air/fuel mixing.

The measurement techniques used were mainly direct measurements from images and no local species information could be obtained. This work will extend previous studies by providing local species concentration information. As noted before, LIBS does not require seeding the flow and can quantify mixing enhancement results through local air/fuel measurements.

CHAPTER 3 APPARATUS AND CALIBRATION

3.1 Calibration

The intensity of the helium atomic emission line in LIBS spectra should increase with the concentration of helium in a sampled volume. To accurately determine the percentage of helium present in the sampled volume, the correlation between helium concentration and signal strength must be determined. Using known concentrations of helium in air, experiments were done to characterize the helium signal response to LIBS.

Three calibration tests were performed to experimentally determine the relationship between the helium signal and helium concentration. Measurements of helium intensity at 588 nm were compared with the intensities of oxygen and nitrogen at 777 and 746 nm respectively, for a given helium concentration. The oxygen and nitrogen emission intensities decreased as the helium concentration increased.

To validate the results, experiments were performed using a helium jet diffusing into co-flowing air. Samples were taken at various heights and distances away from the centerline of the jets. The setup was modeled using FLUENT and theoretical solution curves and the results were compared to the experimentally determined concentrations.

3.2 LIBS Setup

The experimental apparatus consisted of a 31.75 mm ID circular tube into which helium and air were introduced at specified flowrates. Flowrates were controlled and measured using a Drycal DC-Lite digital flowmeter. A Quantel Brilliant Q-switched Nd:YAG laser, operated at the 1064 nm fundamental wavelength, created a small spark directly above the tube's exit at 10 Hz. The laser power, approximately 4 W/pulse, was constantly monitored to avoid any large-scale fluctuations.

The laser beam first is expanded from 5 mm to 22 mm using an appropriately matched lens pair in a Galilean telescope. The expanded beam passes through a hole in a pierced mirror, and is focused into the sample region using a 10 cm focal length fused silica lens. The lens causes the beam to converge and generate a plasma. Light emitted from the plasma is collected by the same fused silica lens and sent to the reflective side of the pierced mirror. The emission is reflected by the pierced mirror to an achromatic collection system (Multichannel Instruments CC-52) which couples the plasma light into a UV-compatible optical fiber. The fiber transmits the light to a Roper Scientific PI-Max gated, intensified CCD camera mated to a 0.3-m Acton SpectraPro 300i spectrometer, from which it is downloaded to a computer using Roper WinSpec software. A diagram of this setup can be seen in Figure 2. The effective dispersion of the system using a 600 groove-mm grating is approximately 0.125 nm / pixel.

The helium measurements were taken with an ICCD shutter delay of 0.1 μs after the laser Q-switch, and a gate (shutter open) width of 5 μs . Nitrogen and oxygen measurements had a delay of 3 μs and a gate width of 15 μs . The atomic emission is highly sensitive to detector timing as discussed in Fisher et al. [34].

Calibration experiments are performed in room 0136A of the Glenn L. Martin Engineering building on the University of Maryland, College Park campus. The pressurized air comes directly from the shop air provided throughout the building. The helium is ordered from Airgas and is certified 99.7% pure.

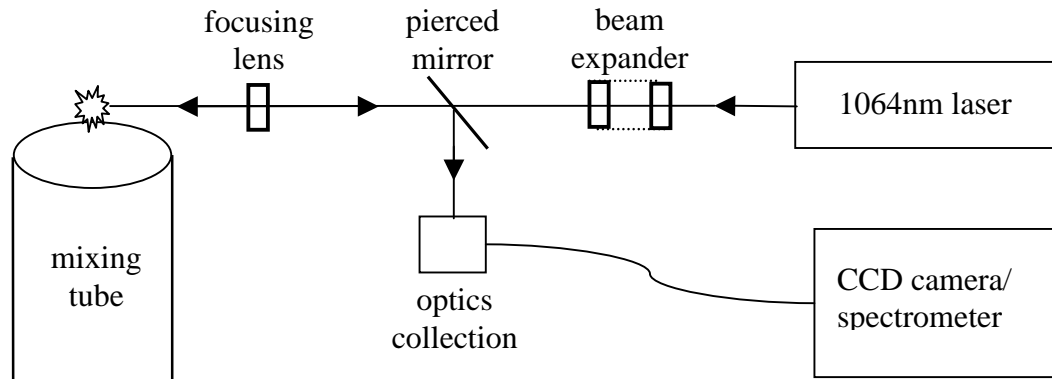


Figure 2 – LIBS data collection setup.

It is important to let the laser reach its normal operating temperature before any measurements are taken. The laser power is monitored at a set flashlamp excitation voltage until the power change over 5 minutes is less than 0.1 Watt. This process takes an average of 35 minutes and ensures a relatively constant laser power for the duration of an experiment.

The calibration tests began with 0% helium when characterizing the helium, oxygen, and nitrogen signals at different concentrations. At a constant total flowrate, the percentage of helium was increased approximately 5% by adjusting the two flowrates between each set of measurements until 100% helium was reached. Secondary measurements were taken at various percentages, such as 10%, 30%, and 65%, and compared to the initial results to check for hysteresis. These secondary tests always agreed with the initial tests, showing that there was no build-up of helium in the surrounding area during the test or errors in the flow meters.

Two sets of measurements were taken at each concentration level, one spanning 679.9 – 808.2 nm to record nitrogen and oxygen signals and another spanning 521.2 - 653.58 nm for the helium signal. To reduce the noise, 300 single shot calibration measurements were averaged into three spectra of 100 shots each. As discussed before, averaging over 100 shots reduces random noise by $N^{-1/2}$, where N equals the number of measurements.

During the annular tube experiment, the flowrates are initially set to match the two jet velocities and remained unchanged throughout. The tube assembly is mounted on two traversing stages for axial and radial translation. The same process of measuring 300 shots of helium, then 300 shots of oxygen and nitrogen is used. After each set of measurements, the annular tubes are moved at 2 mm intervals to the next sample point.

The data files are displayed graphically as the tests are run, showing intensity vs. atomic line (nm). The data is stored temporarily as a Winspec file then it is converted to a text file using the WinSpec software tools. Matlab m-files import and process the data as discussed in Chapter 5. The peak-to-base values are calculated from the intensities of the helium, oxygen, and nitrogen signals. For helium, the peak is integrated from 585 to 588 nm and divided by the area under the featureless region between 547 and 560 nm, see Figure 3. When calculating oxygen and nitrogen intensities, the peaks are integrated from 773 to 778 nm and 744 to 748 nm respectively then divided by the area between 722 and 734 nm, see Figure 4.

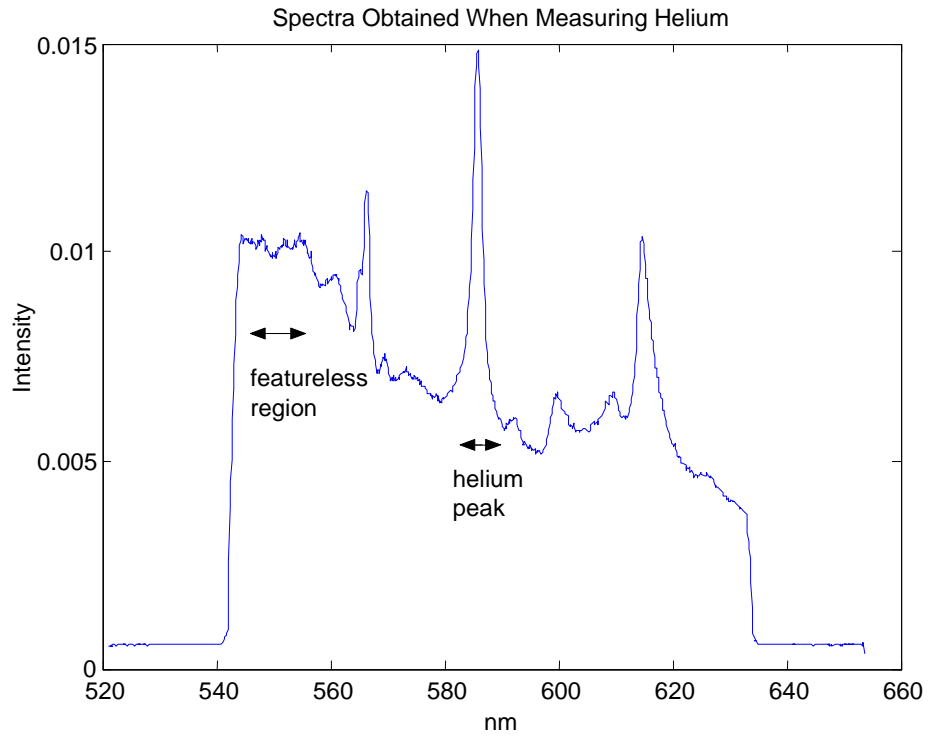


Figure 3 – Example spectra when measuring helium intensity at 588 nm.

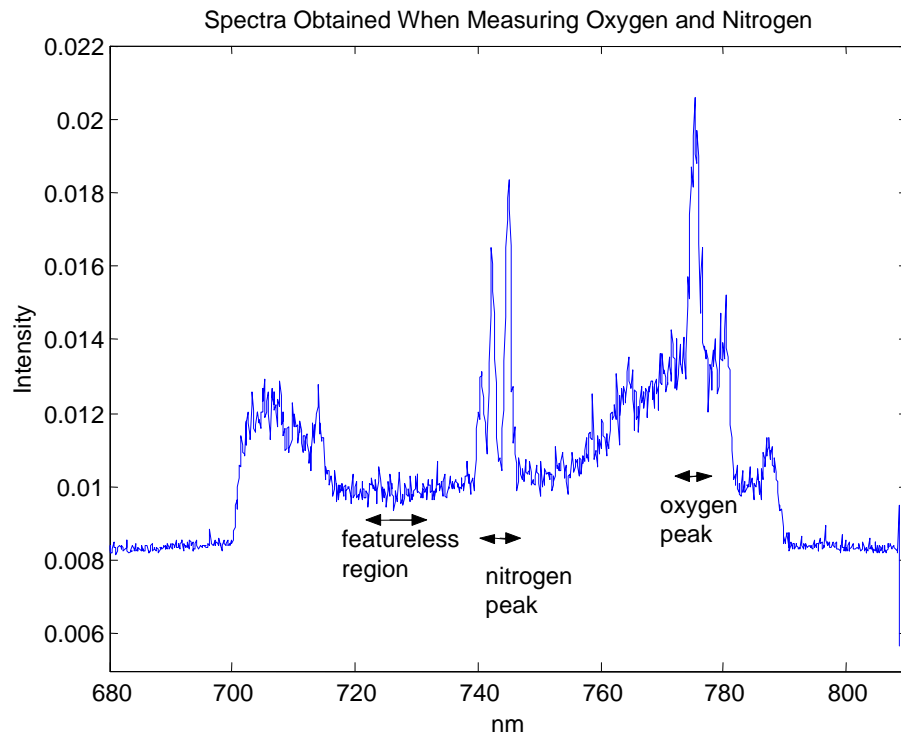


Figure 4 – Example spectra when measuring oxygen and nitrogen.

Figures 3 and 4 also show that there is a positive intensity value at every wavelength. The sum of the area under the peak for each element will always have a positive value. The featureless region used as the base will always have a positive value as well. Because both the peak and base have positive values, the peak-to-base signals for each element are not equal to zero when none of that element is present. For the peak-to-base value to equal zero when none of the element is present, the smallest peak-to-base value can be subtracted from the peak-to-base curve, but this step is omitted here for simplicity. Because of the presence of this baseline offset, the peak-to-base ratio is actually calculated as the sum of the peak and base divided by the base. This does not fundamentally change the results, but does ensure that data values are positive.

3.3 Initial Calibration

Measurements were taken at the four strongest atomic emission lines of helium: 447, 588, 668, and 706 nm. The peak-to-base ratio was calculated at each of the four atomic lines for helium concentrations varying from 0 – 55%. The results from these experiments can be seen in Figure 5. The 588 nm atomic line proved to be the strongest signal with the best sensitivity level and therefore was used in all subsequent experiments. Figure 6 shows the 588 nm intensity with error bars of $\pm 2 \sigma$, where σ is based on three 100-shot ensemble-averaged measurements.

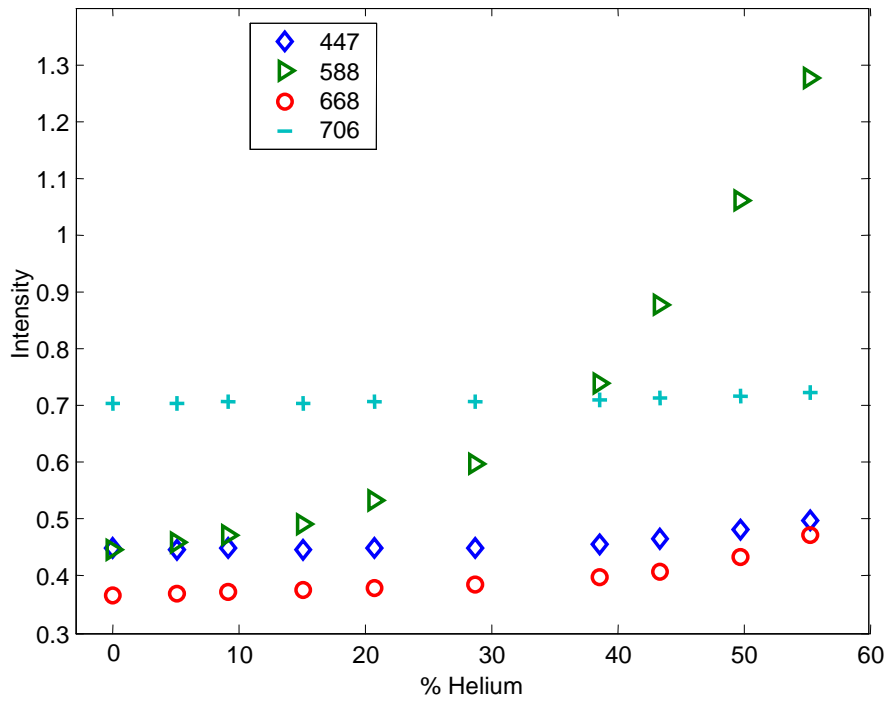


Figure 5 – Helium peak-to-base intensity at the four main wavelengths.

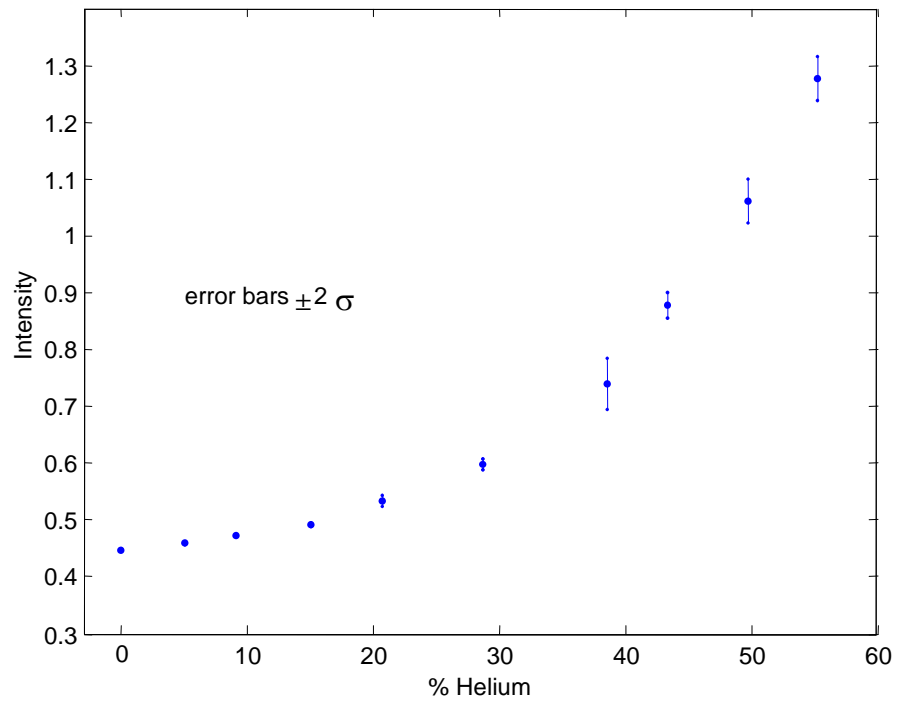


Figure 6 – Peak-to-base intensity of helium at 588 nm with error bars.

During these experiments it was observed that the overall intensity of the spark decreases as the percentage of helium increases. As noted previously, this is attributed to the higher ionization potential and thermal conductivity of helium. When the helium percentage exceeds 80%, any further increase in the intensity of the helium signal at 588 nm is offset by the decrease in plasma intensity, causing a non-monotonic variation of intensity with helium concentration. The concentration can be measured accurately below the limit of 80%. An example of the helium peak-to-base intensity from 0-100% can be seen in Figure 7.

One possible solution to the helium signal quenching would be to use the oxygen or nitrogen intensity and find a ratio between the two elements. Even though the helium signal may not increase, the oxygen and nitrogen signals continue to decrease above 80% helium. The LIBS signal response for nitrogen (746 nm) and oxygen (777 nm) were found at different helium concentrations. Both signals responded almost exactly the same way, though the oxygen signal had a greater negative slope over the range of measurements. This can be seen in Figure 8.

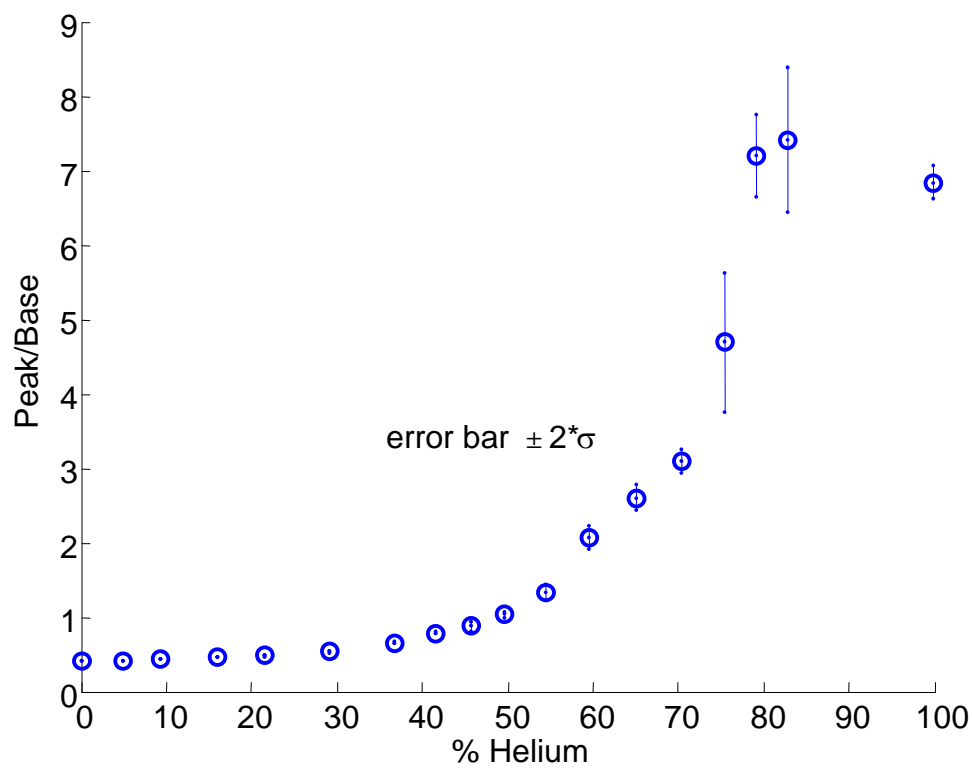


Figure 7 – Helium peak-to-base values at 588 nm.

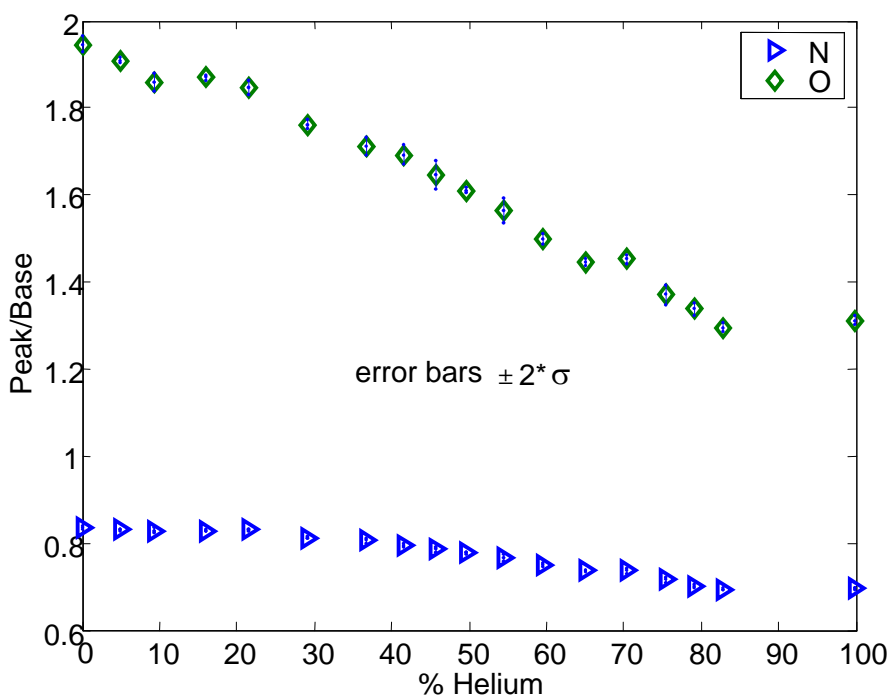


Figure 8 – Oxygen and nitrogen peak-to-base intensity as a function of % helium.

In three experiments, three separate sets of 100 oxygen and 100 helium measurements were taken at each point. The 300 oxygen and 300 helium measurements were averaged and provided three separate sets of oxygen / helium data which can be seen in Figure 9. A curve was fitted to one of the experimental O / He data sets using the *polyfit* command function in Matlab. Each curve was estimated using a second-order and a fourth-order equation. A fourth-order equation of the last data set was chosen because it had the smallest mean residual values compared to the curve fits for the other sets of data. The legend provides the average square of the residuals between the data fit and the experimental values which indicates the error that may occur between different sets of data.

From the curve fit it appears possible to calculate helium percentage accurately below 75% once the oxygen and helium peak-to-base values are known. For single shot data, simultaneous measurement of both elements is required. Unfortunately, due to the limitations of helium quenching, the oxygen / helium ratio can not accurately predict helium concentration above 75%.

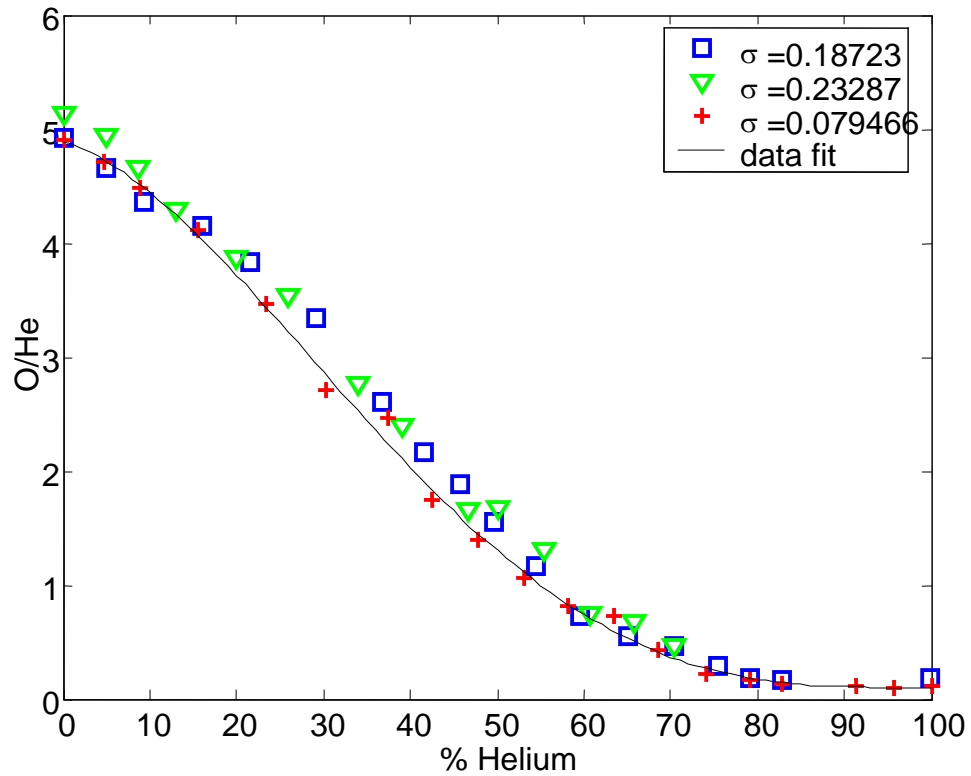


Figure 9 – O / He ratio from three different experiments.

The normalized residuals for the three sets of experimental values are plotted in Figure 10. There are four distinct regions where the normalized residual value is similar: 0-25% helium, 25-45% helium, 45-75% helium and 75-100% helium. The normalized residual was calculated using Equation 1. Figure 11 shows the fractional error determined from the total number of measurements in each concentration range, see Equation 2, and the estimated fractional error values for each range are displayed in the legend. The estimated total error was determined from Equation 3 and is shown in Figure 12 along with the experimental values.

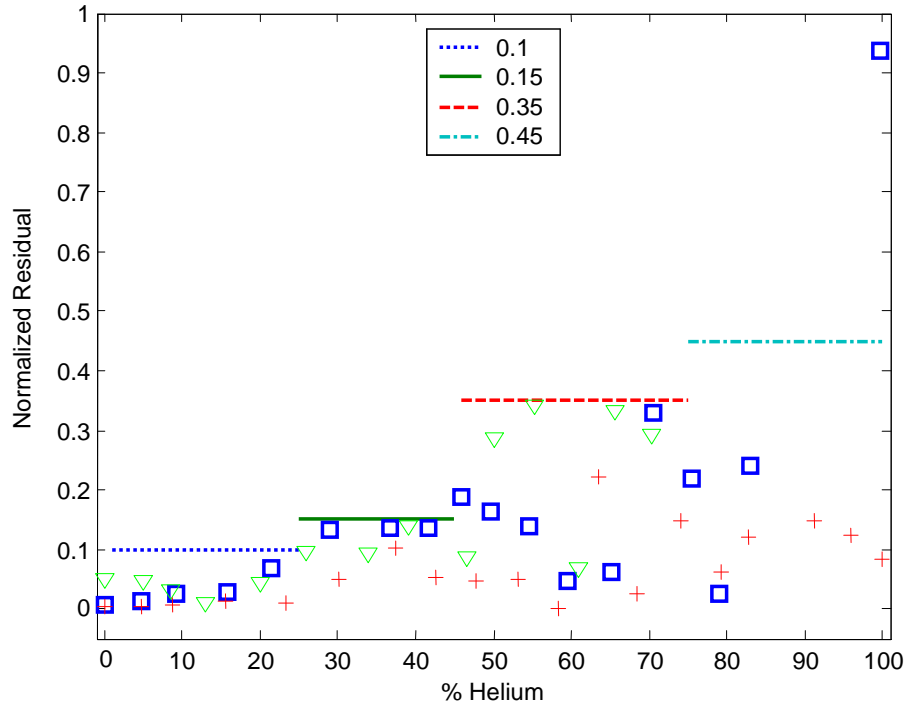


Figure 10 – Normalized residual between the three characterization experiments and the data fit.

$$R_N = \left\| \frac{(X_{data} - X_{fit})}{X_{data}} \right\|$$

R_N	Normalized residual
X_{data}	Experimental data value
X_{fit}	Data fit value

Equation 1 – Normalized residual for the three sets of experimental data

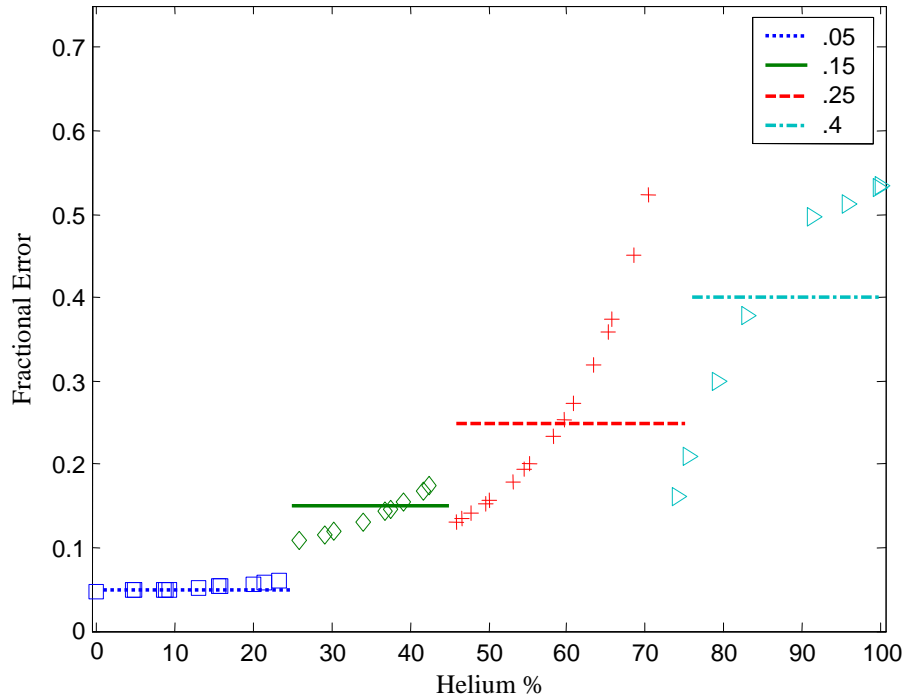


Figure 11 – Fractional error at four different concentration ranges.

$$FE_j = \frac{\sqrt{\frac{1}{N_j - 1} \sum_1^{N_j} (X_{data} - X_{fit})^2}}{X_{fit}} + \delta_{flowmeter}$$

FE_j	Fractional error in each range
N_j	Number of data values in each range
X_{data}	Experimental data value
X_{fit}	Data fit value
$\delta_{flowmeter}$	Error in flowmeter measurement

Equation 2 -- Fractional error for the four different concentration ranges.

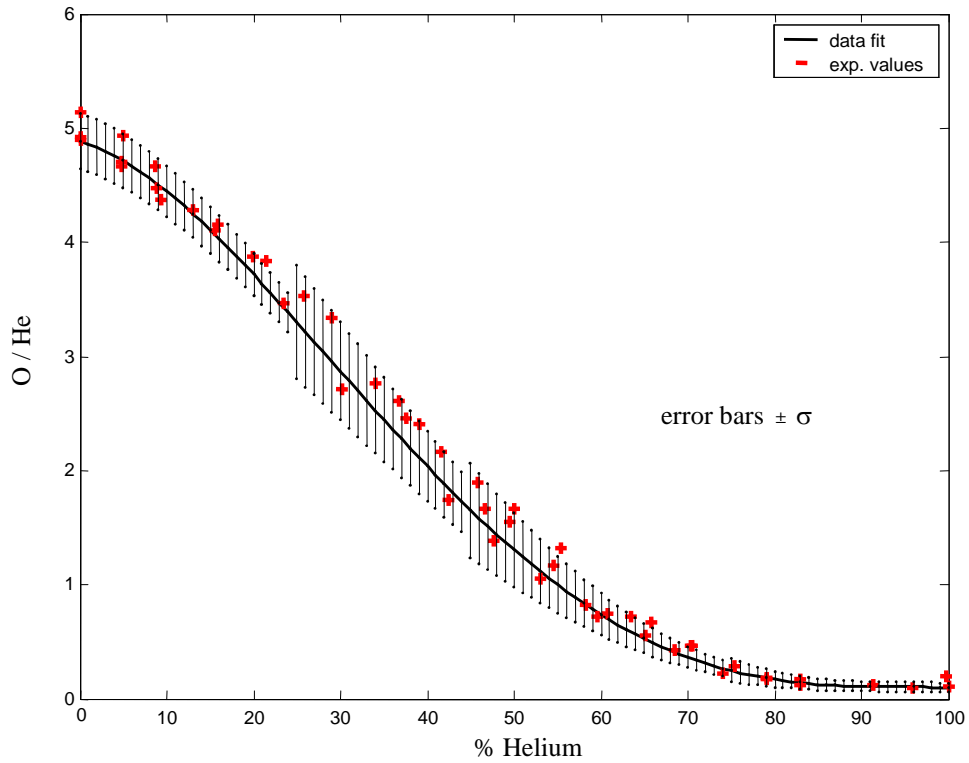


Figure 12 – Data fit curve with the total error in each concentration range with the experimental values.

$$TE_i = FE_j \times X_{fit}$$

TE_i	Total error at each point
FE_j	Fractional error in each range
X_{fit}	Data fit value

Equation 3 - Total error in each concentration range.

3.4 Annular Tubes – Diffusion Experiment

Experiments were performed to validate the calibration data fit in a laminar diffusion, annular jet experiment. The setup was identical to the first set of experiments except that

an inner tube 4 mm in diameter was inserted into the center of the existing tube creating an axisymmetric jet assembly. Measurements were taken at various radial and axial coordinates, see Figure 13, and compared with a Fluent simulation and theoretical solutions. To accurately determine the spark position relative to the jet, the tube assembly was mounted on two traversing stages. Both have a 12 mm range with $\pm .01$ mm accuracy and were mounted for motion in the radial and axial directions.

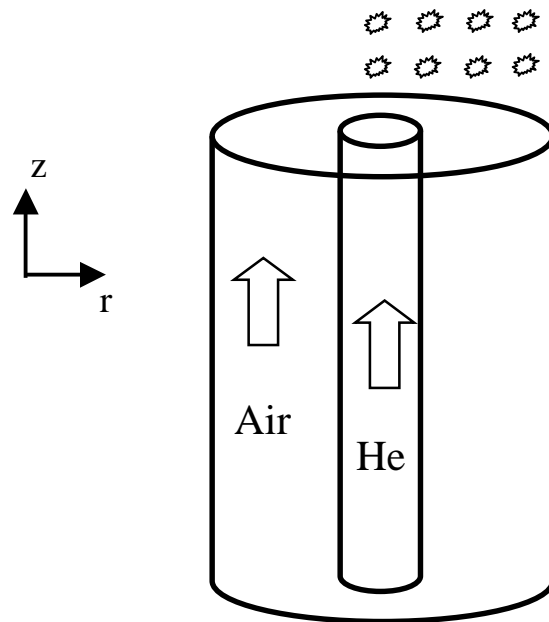


Figure 13 – Spark locations during annular tube experiment.

To minimize the turbulence created by the shearing interaction between the jets, the inner tube is tapered at the exit and the jet velocities were matched. The flowrates for the air and helium jets were 7.95 and 0.56 ± 0.01 L/min respectively, corresponding to a Reynolds number of 110 for air, 3.4 for helium, and a common velocity of 51 mm/s.

The data reveal a shape typical of diffusion curves at various axial heights. Figure 14 shows the O/He ratio, which has a minimum directly over the helium jet centerline ($x =$

0) and becomes uniform after a certain radial distance ($r \sim 5$ mm), at several axial distances. As height above the jet increases, increased oxygen diffusion into the center of the helium jet is observed. The error bars are determined from the sum of the fractional error of the oxygen and helium signals, where the fractional error is calculated using Equation 4. The O/He values can be interpreted using the calibration curve obtained in Figure 9. The *interp1* function in Matlab is utilized for this step and the results can be seen in Figure 15. The sum of the fractional error in oxygen and helium measurements and the fractional error in the data fit curve were summed to calculate the total error in measuring the helium concentration. The value of the O / He intensity dictated which helium concentration range, hence which data fit fractional error value, to use at each point. A more complete discussion of the error involved in these measurements can be found in Chapter 5, error bars shown on Figure 14 and Figure 15 are $\pm 2\sigma$.

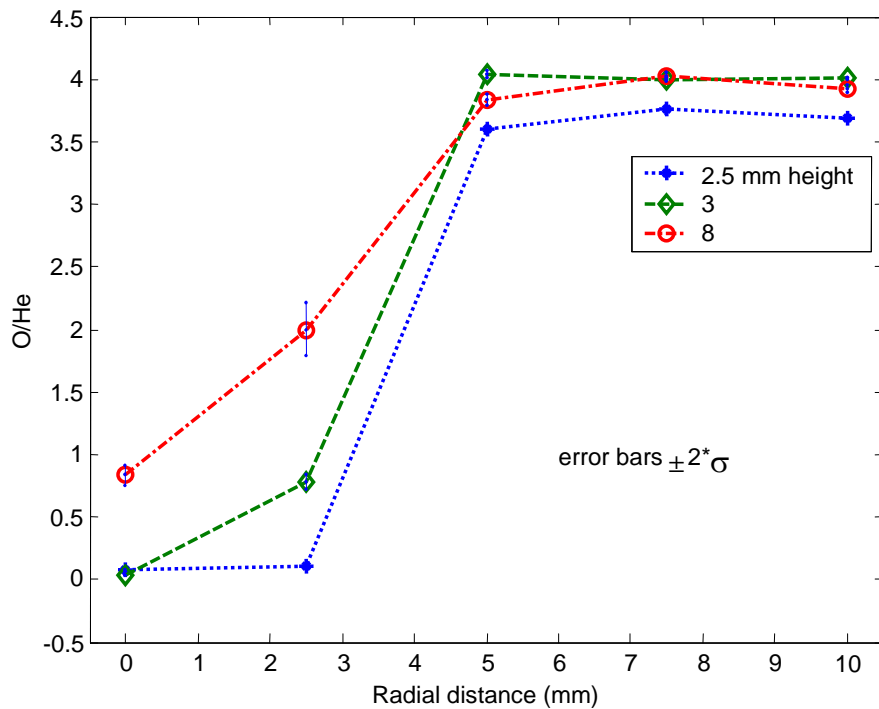


Figure 14 -- Oxygen / helium ratio at various axial distances.

$$FE = \frac{\sqrt{\frac{1}{N-1} \sum_1^N (X_{data} - X_{mean})^2}}{X_{mean}}$$

FE	Fractional error
N	Number of averaged measurements
X _{data}	Intensity value from measurement
X _{mean}	Average intensity value

Equation 4 -- Fractional error for both helium and oxygen during the annular tube experiment.

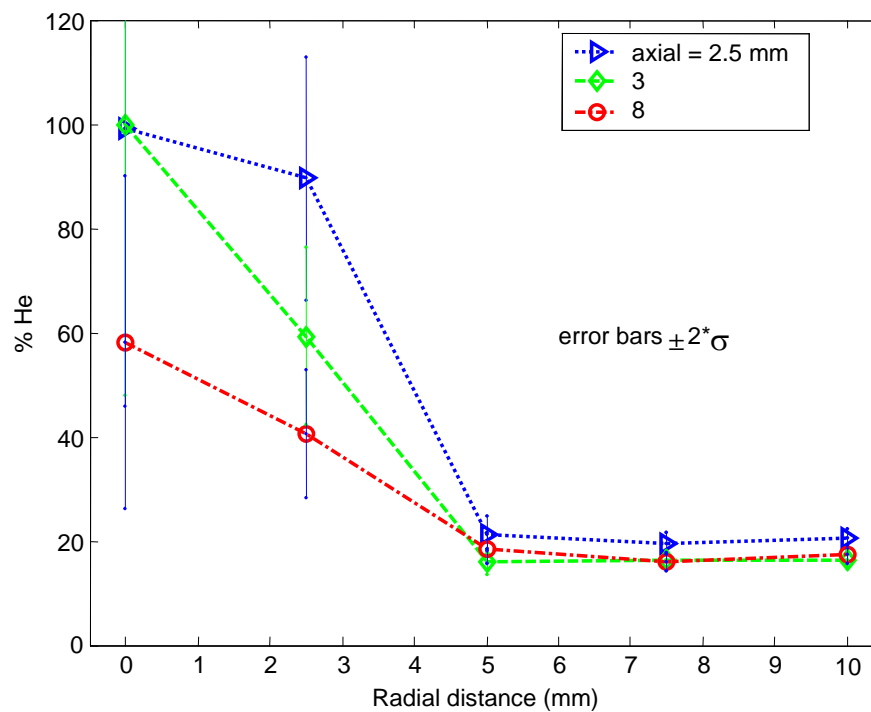


Figure 15 – Volumetric helium percentages at several axial distances.

3.5 Fluent Simulation

The fluid dynamics package FLUENT was used to solve transport equations of this binary mixture. The experiment is axisymmetric, allowing a solution on a 2-D mesh. A laminar calculation was performed because the jets are velocity-matched and the Reynolds number based on the outer tube diameter is approximately 110. The 2-D solution area was created in Gambit with fine boundary layer meshes at the entrance of the helium jet and along the axis of symmetry. The mesh was refined until the change in node values varied less than 2 % from one refinement to the next.

The assumptions and restrictions on the FLUENT model lead to inaccuracies in the simulation. The helium and air are assumed to have a constant velocity that is normal to the jet exit plane, but this is not completely accurate where the two jets begin mixing. A more accurate simulation would use a velocity profile corresponding to fully developed pipe flow because of the no-slip condition at the walls.

The simulation was also based on the hydrogen-air mixture template already present in Fluent, as there is no helium-air mixture template. The molecular weight of hydrogen was set equal to that of helium so diffusion coefficients should be similar, since FLUENT calculates diffusion coefficients based on the molecular weight. The co-flowing air was set to a mixture of 22% oxygen (O₂) and 78% nitrogen (N₂) by volume.

The data was exported from FLUENT as either the mole fraction or mass fraction of H₂ on the y-axis and the radial coordinate on the x-axis. The mass fraction values obtained in FLUENT can be seen at several axial heights in Figure 16. The slight discontinuities in the FLUENT profiles can be attributed to the non-uniformity in the mesh distribution near the axis of symmetry.

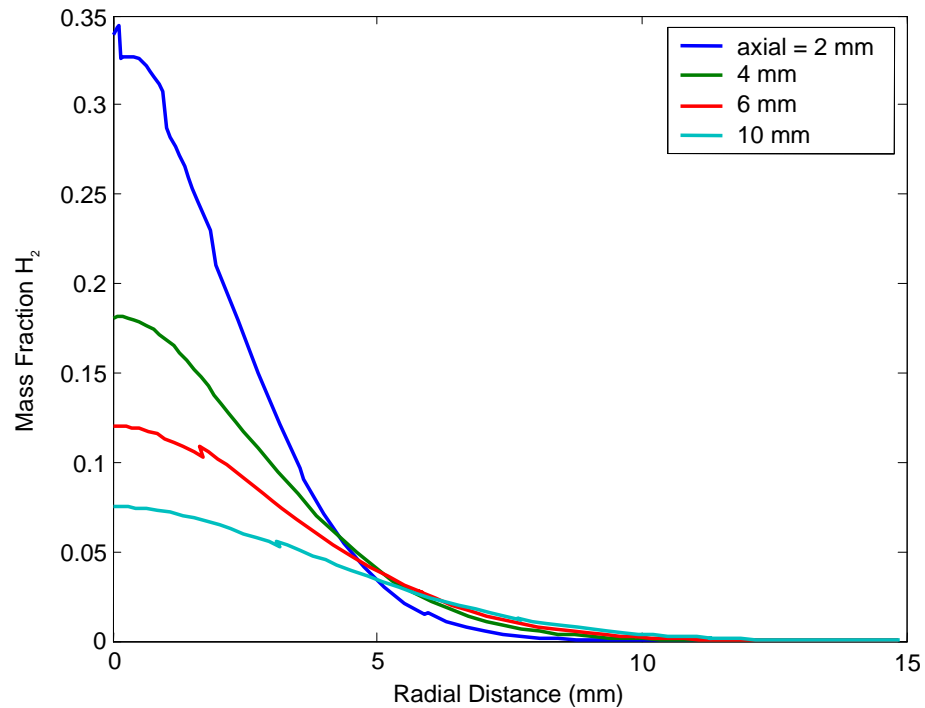


Figure 16 – Mass fraction of H₂ at various axial heights, obtained from FLUENT simulation.

A comparison of the results from the CFD model and the LIBS measurements and can be seen in Figure 17. Though the general shape and distribution profiles for mass fraction look similar, the absolute values from the experiments do not match the simulation. Beyond the uncertainties in the FLUENT simulation described above, these discrepancies could also be due to several experimental reasons, such as turbulence caused by the laser spark interfering with the laminar diffusion of helium, or factors affecting the experimental environment such as drafts created by nearby vents. It is also difficult, if not impossible, to compare the results from the FLUENT simulation to measured concentrations of helium greater than 75% by volume, which relates to a helium mass fraction > 0.3 .

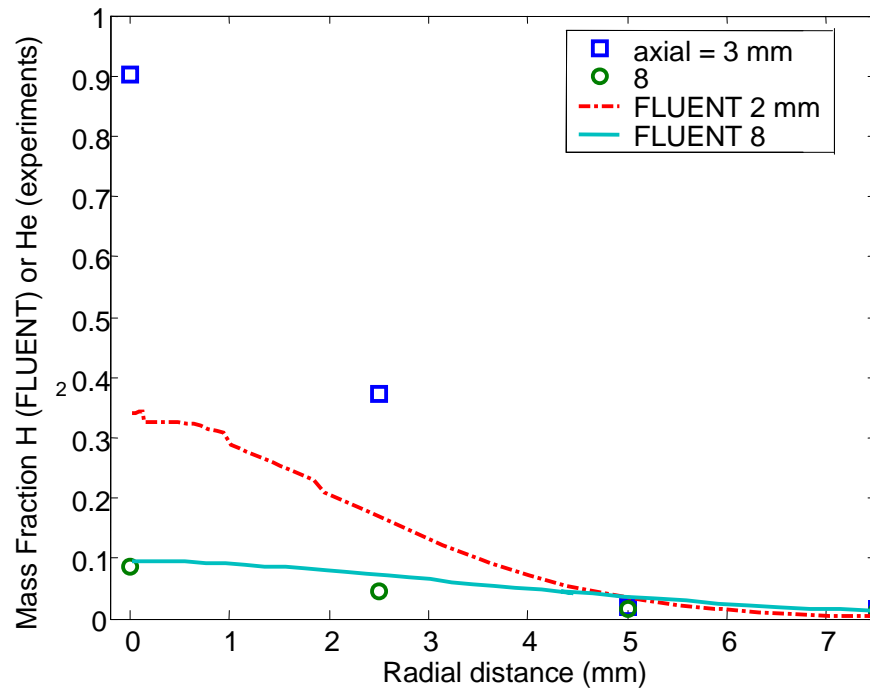


Figure 17 – Experimental results compared with CFD results from FLUENT.

3.6 Theoretical Normalization

Dyer [33] made similar concentration measurements with propane in a turbulent ($Re = 9790$) axisymmetric jet assembly. Mean concentrations of propane along the radial axis at three different heights were all shown to correlate well with a Gaussian curve fit. It was noted that the “data may be readily collapsed to a single curve by normalizing the propane mole fraction by its centerline value and normalizing the radial coordinate r by $R_{1/2}$, the position where the concentration has dropped off to one-half the centerline value.”

The method of Dyer is an additional method for validating the results of the annular tube experiments. The suggested normalization process was performed on the mass fraction values obtained from FLUENT and the data collapsed well, as shown in Figure 18.

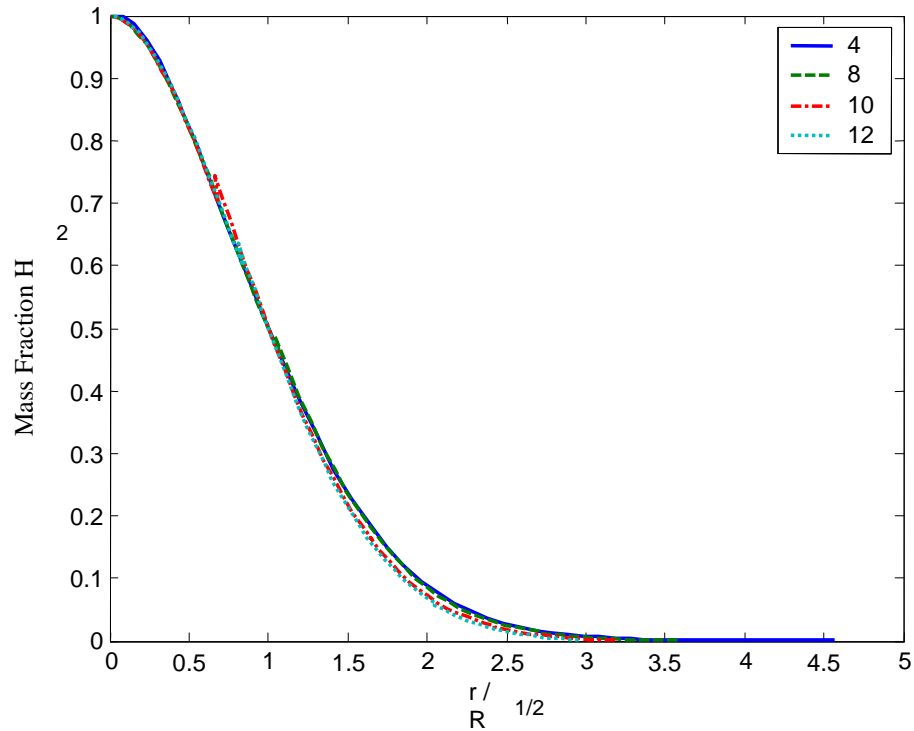


Figure 18 – Normalized mass fraction data obtained from FLUENT.

The experimental results would be expected to deviate from a single curve due to the errors discussed in the previous section, especially the limitation in measuring high percentages of helium. This would skew the results when using the centerline value to normalize the curve, because the centerline value is above 75% helium in most cases. The normalized data is shown in Figure 19; the data is found to collapse moderately well.

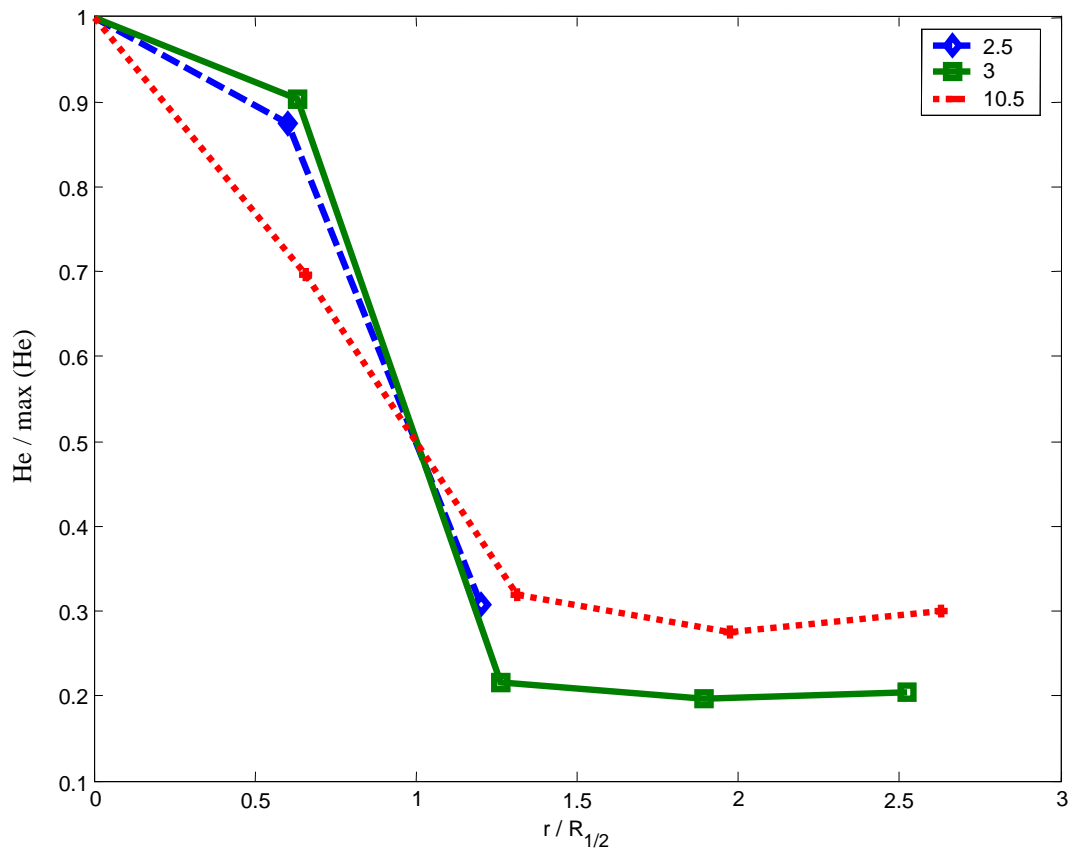


Figure 19 -- Normalized helium concentration curves obtained through experiments.

3.7 Calibration Data Summary

The helium / oxygen intensity ratio was found to be accurate and repeatable in three separate experiments. A calibration curve, as in Figure 9, can be fitted to the data to calculate helium percentage in future experiments. The calibration experiments show that the concentration of helium can be measured with a conservatively determined $\pm 5\%$ fractional error for 0-25% helium, $\pm 15\%$ fractional error for 25-45% helium, $\pm 25\%$ fractional error for 45-75% helium, and $\pm 40\%$ fractional error for 75-100% helium.

Validation of the calibration curve was attempted through measuring the diffusion profile in coaxial jets of helium and air. Due to the lack of data from previous helium

diffusion experiments, a FLUENT simulation and a theoretical normalization model were used for validation. In part because of FLUENT modeling limitations and due to measurement uncertainties at high helium concentrations, the values obtained from FLUENT and the theoretical solutions did not completely agree with the experimental data.

The results from the annular tube experiments and the initial characterization show that the LIBS signal intensity is dependent on the amount of helium present. The correlation between the concentration of helium and the oxygen / helium peak-to-base intensity can be represented with a 4th order curve-fit. The best resolution for this model is below 25% helium and the fractional error increases with increasing helium concentration. The helium signal is quenched above 75% concentration and the helium and oxygen LIBS signals can not be accurately used to determine helium concentrations above this level.

CHAPTER 4 EXPERIMENTAL WIND TUNNEL RESULTS

4.1 Experiments

The laser and optical setup were taken to a supersonic wind tunnel facility in the Engineering Lab Building. Baseline experiments were performed without a mixing cavity and a second set of tests were completed with a mixing cavity. Helium and oxygen measurements were taken at a total of nine different points downstream from the helium injector port at three separate gauge pressure combinations.

The wind tunnel apparatus has been described in great detail in prior publications [29]. Pressurized air is provided from an Atlas Copco compressor. The air is sent through a dryer to remove moisture and a gas/air filter to remove residual oil before being sent to the laboratory. A 2 in. diameter pipe connects the compressed air source to an adapter plate with a square cross-section. A pressure transducer is mounted in this pipe which provides a measurement of the upstream gauge pressure. The adapter plate, made of stainless steel, connects the compressed air to the front of the wind tunnel assembly. The sides of the wind tunnel are quartz to allow measurements requiring optical access. The bottom wall of the wind tunnel contains the cavity. The nozzle located upstream of the cavity is designed for a Mach number of 2.059 at the exit. The wind tunnel, with a close-up of the test section, can be seen in Figure 20.

Helium is injected through a 4 mm diameter opening 6.5 mm downstream of the cavity. The injection port is located in the wake of the cavity so the incoming fuel becomes entrained in the large, coherent structures. The center of the helium injector lies along the centerline of the wind tunnel, ensuring symmetric conditions. A pressure

regulator monitors the gauge pressure of the helium and an electronic valve controls the flow.

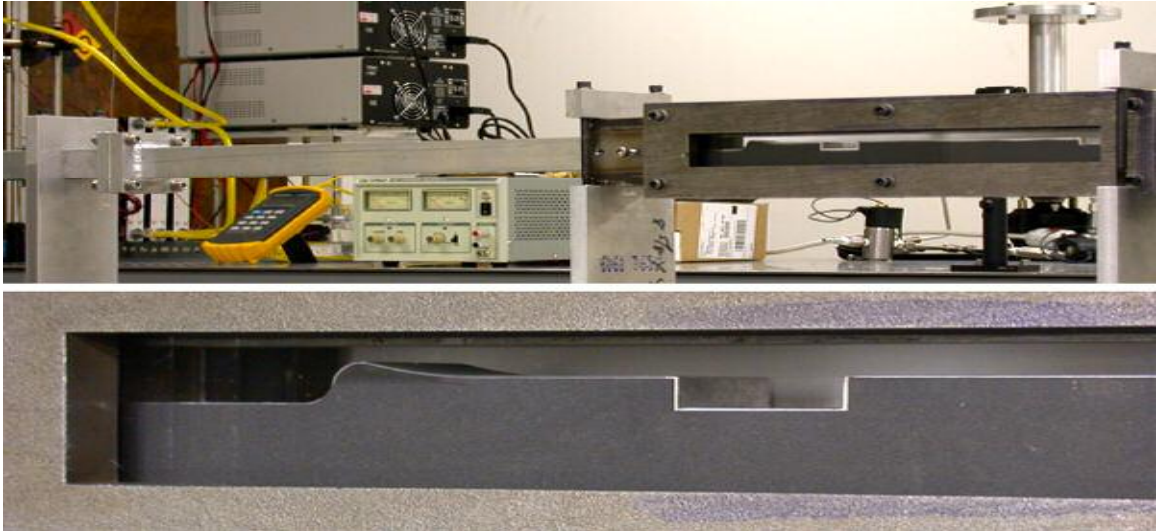


Figure 20 – Wind tunnel setup with close up of cavity test section.

The laser and focusing optics were mounted on a cart at the side of the wind tunnel. The pierced mirror setup, refer to Figure 2 in Section 3.2, ensured a constant alignment between the plasma and the center of the collecting optics, regardless of the refraction cause by the quartz window.

Additional tests were performed with the pierced mirror rotated slightly to focus 1-5 mm downstream of the plasma. The results of these tests show that even when centered 5 mm downstream, the area monitored by the collection optics still contains the initial stages of the plasma. The collection optics do not have to be centered exactly on the spark and in future experiments an incident-angle collection, instead of a pierced mirror, can be utilized.

Measurements are taken along the centerline of the wind tunnel, considered $y = 0$. Measurements were also taken at $y = -5$ mm and $y = -10$ mm. The first set of points is $x = 6.3$ mm downstream of the injector port and two more sets were taken at $x = 31.7$ mm and $x = 57.1$ mm downstream, with $x = 0$ at the center of the helium injector. All measurements were taken at a constant height of 3.2 mm from the wind tunnel floor. See Figure 21 for a detailed representation of measurement locations.

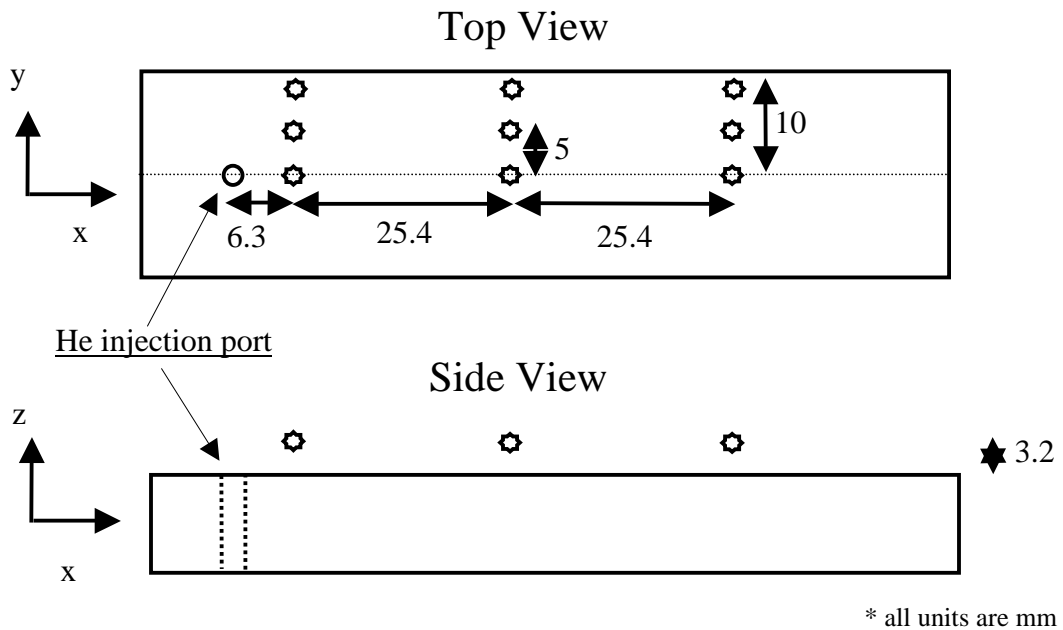


Figure 21 – Placement of measurement points during wind tunnel experiments.

4.2 Calibration

Nine different combinations were considered when determining the optimum gauge pressures for helium and air. Changing the air pressure has no effect on the velocity of the air; it only changes the mass flow rate through the tunnel chamber. Increasing the helium pressure does change the exit velocity of the helium, causing a larger amount of penetration into the supersonic flow. To determine the extent of helium penetration, the spark was positioned along the centerline of the wind tunnel, 6.3 mm behind the helium

injection point, and 3.2 mm up from the bottom wall. Additional measurements were taken at $y = 5$ and -5 mm from the centerline. The baseline wall, without a cavity, was used in this experiment.

The gauge air pressure was set to 20, 50, and 90 psi while maintaining gauge pressures of helium at 20, 40, and 60 psi respectively. Results showed that the helium signal was negligible for all cases of air greater than 20 psi. With 20 psi air pressure, the strongest helium signals were recorded when helium was 40 psi and 60 psi. Three different inlet gauge pressure combinations were used for the experiments with and without the cavity: air at 20 psi with helium at 40 psi, air at 20 psi with helium at 60 psi, and air at 40 psi with helium at 60 psi. The helium signals can be seen in Figure 22 for the two strongest cases.

Single-shot spectra were taken during all of the wind tunnel experiments to allow a more detailed analysis of the turbulent characteristics of the flow. At each point, 100 uncorrelated measurements were recorded for both oxygen and helium spectra. The peak-to-base intensity for oxygen and helium is determined from each of their 100 spectra, and the standard deviation of the peak-to-base measurements are used to calculate the error bars in Figure 22, Figure 23, Figure 26, Figure 31, Figure 32, Figure 33, and Appendix B – Graphs from Wind Tunnel Experiments.

Values obtained in this experiment may have very large fluctuations due to the turbulence in the flow. The standard deviation of the helium / oxygen value is commonly much larger than the actual value, especially along the centerline where the helium concentrations are highest. Including error bars of $\pm 2 \sigma$ does not represent the data spread accurately since the helium / oxygen value can never be negative, as discussed in

Section 3.2. For this reason, the error bars displayed are only $\pm \sigma$ and figures or tables representing the true distribution of helium / oxygen peak-to-base intensity values are displayed when appropriate.

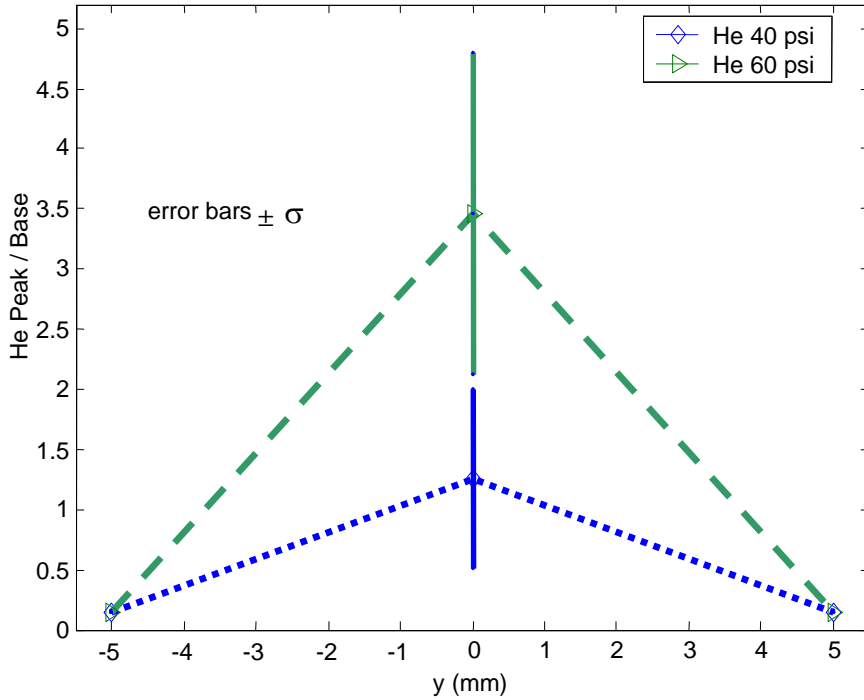


Figure 22 – Helium peak-to-base ratio with air at 20 psi and helium at 40 psi and 60 psi.

4.3 Experimental Results

The results from the tests without a cavity show the strongest helium signal along the centerline at each downstream distance. Figure 23 shows the He / O signal at the three x-axis locations. As the helium diffuses into the supersonic air jet and mixing occurs downstream, the helium spreads outward toward the wall. The graphs of the wind tunnel data show He / O intensities to allow an observer to quickly identify where the helium is most concentrated. Figure 24 shows the actual measurement values of the helium and oxygen peak-to-base intensities at the centerline ($y = 0$) and $x = 6.3, 31.7,$ and 57.1 mm, with averages and standard deviations shown on each plot. Figure 25 shows the same

data as Figure 24 but in histogram form, representing the probability density function of concentration at each point. The first two histograms, when the helium signal is significant, show relatively Gaussian profiles indicating a well-mixed flow.

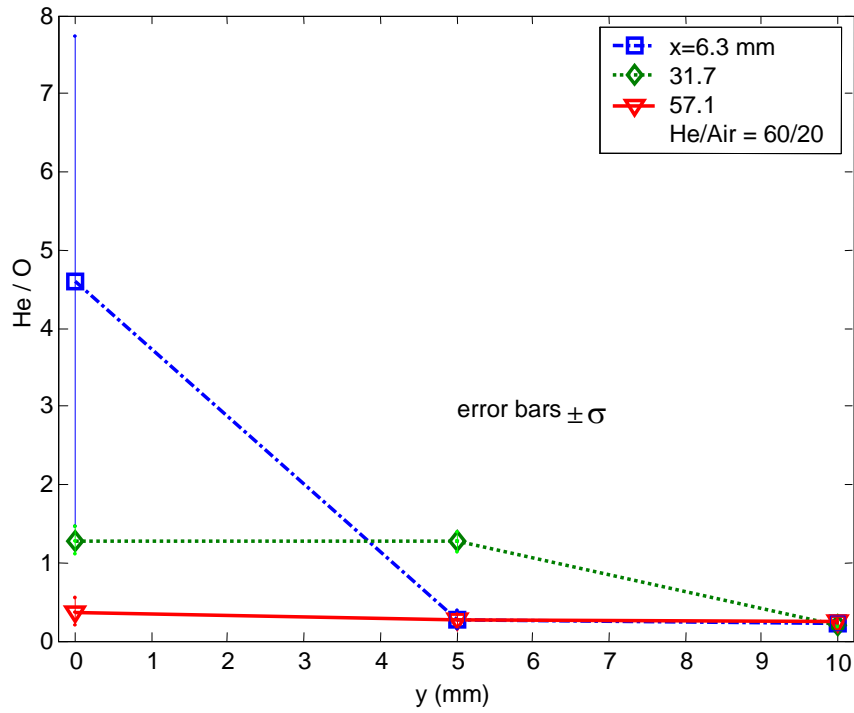


Figure 23 -- He / O intensity ratio at three downstream locations (w/o cavity).

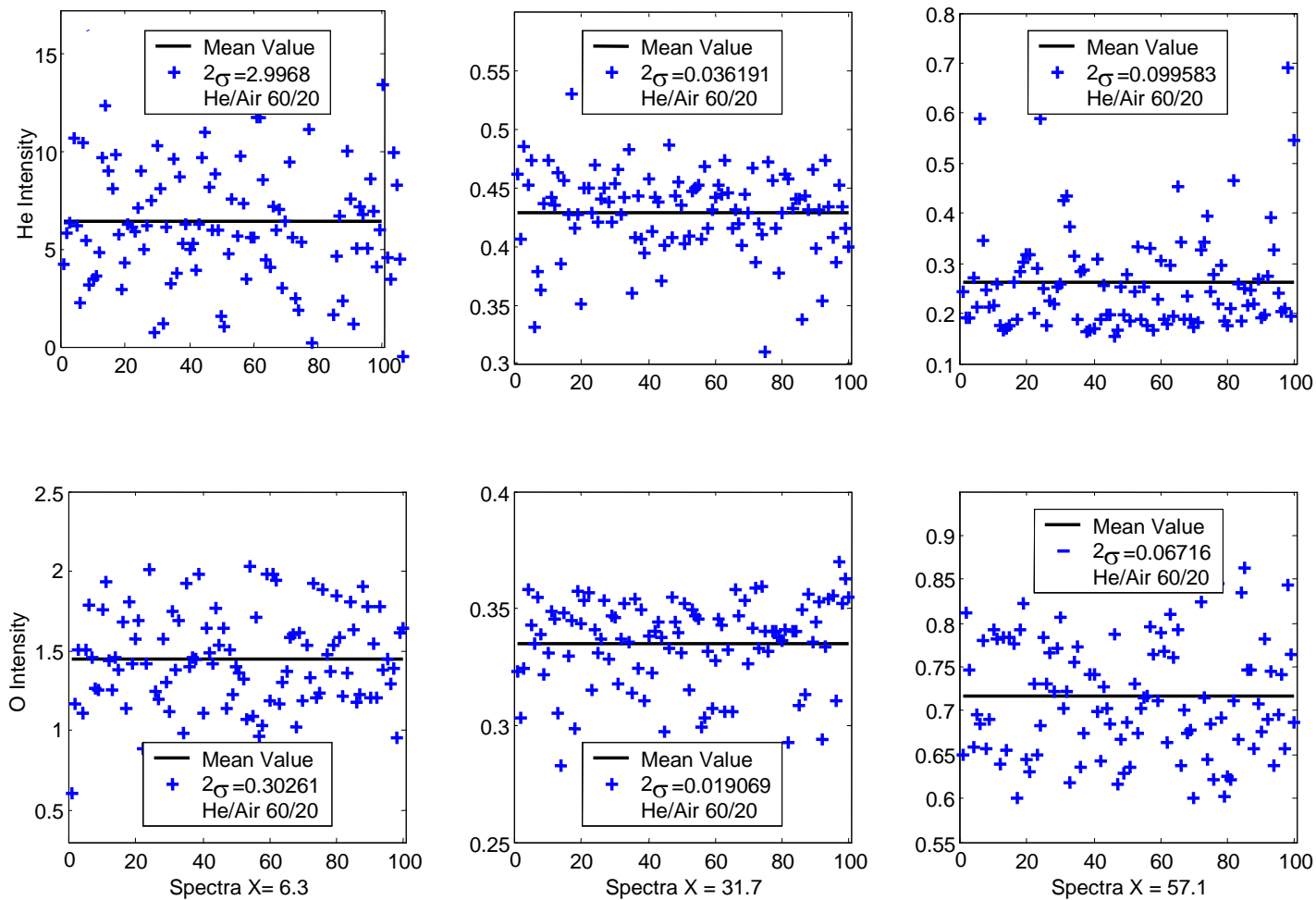


Figure 24 – Single-shot values of He and O intensity at $y = 0$ and $x = 6.3, 31.7,$ and 57.1 mm for the He/Air 60/20 pressure case (w/o cavity).

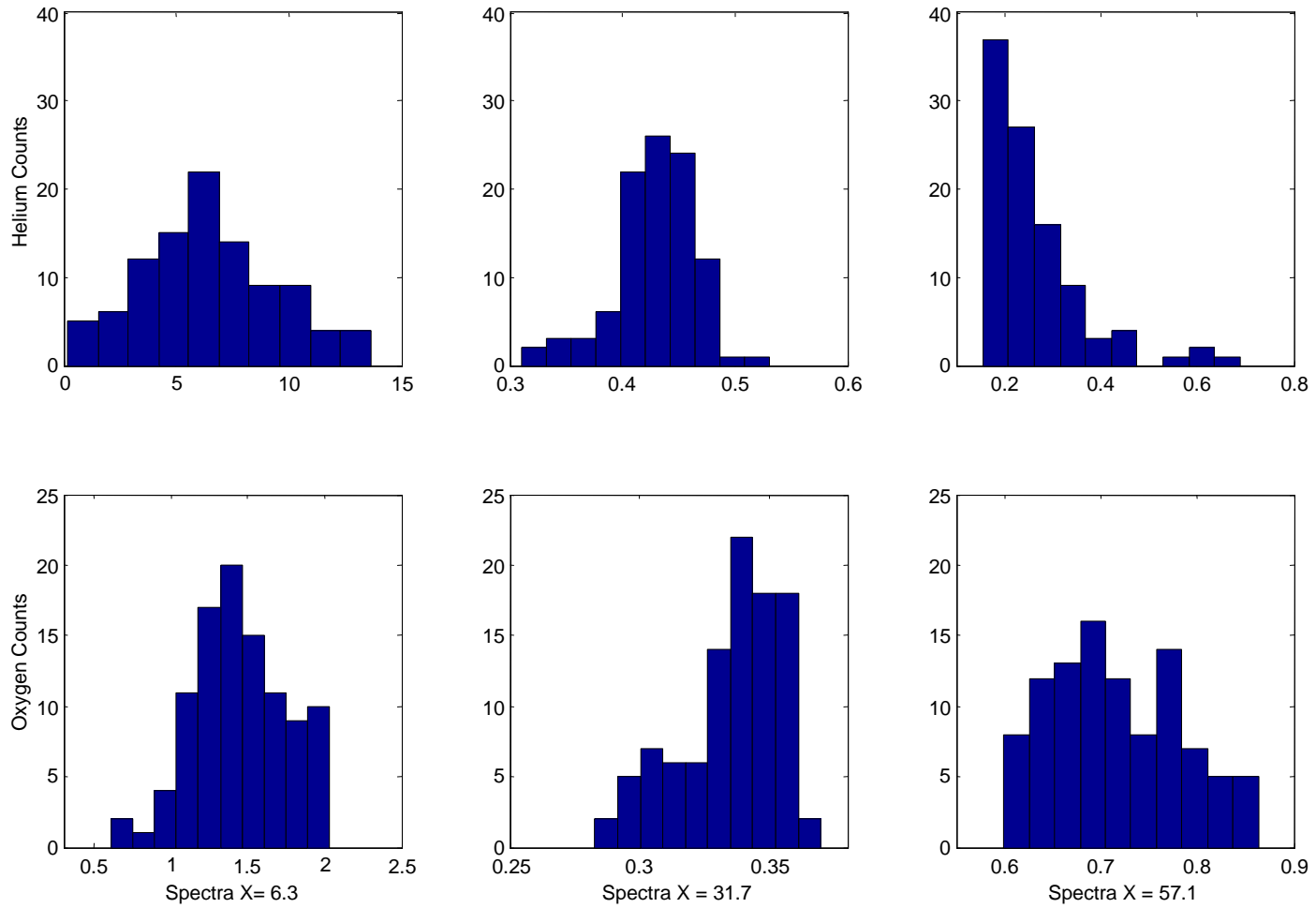


Figure 25 – Histograms of helium and oxygen intensity at $y = 0$ and $x = 6.3, 31.7,$ and 57.1 mm for the He/Air 60/20 pressure case (w/o cavity).

The experiments with the wall cavity showed a similar pattern of diffusion, as shown in Figure 26 for the same inlet pressure conditions as Figure 23. The two experiments agree that the concentration of helium is higher along the centerline and that it diffuses outwards downstream. The main difference between the two is that the cavity experiment showed less helium present at the measured points, presumably due to enhanced mixing in the spanwise and vertical directions. Figure 27 shows the actual distribution of the He / O values at $x = 6 \text{ mm}$ and $y = 0$. Figure 28 shows the same information from Figure 27 but in histogram form. The histograms in Figure 25 and Figure 28 show that the wall cavity causes the overall helium concentration to fall and the data no longer fits a Gaussian curve, indicating more turbulence.

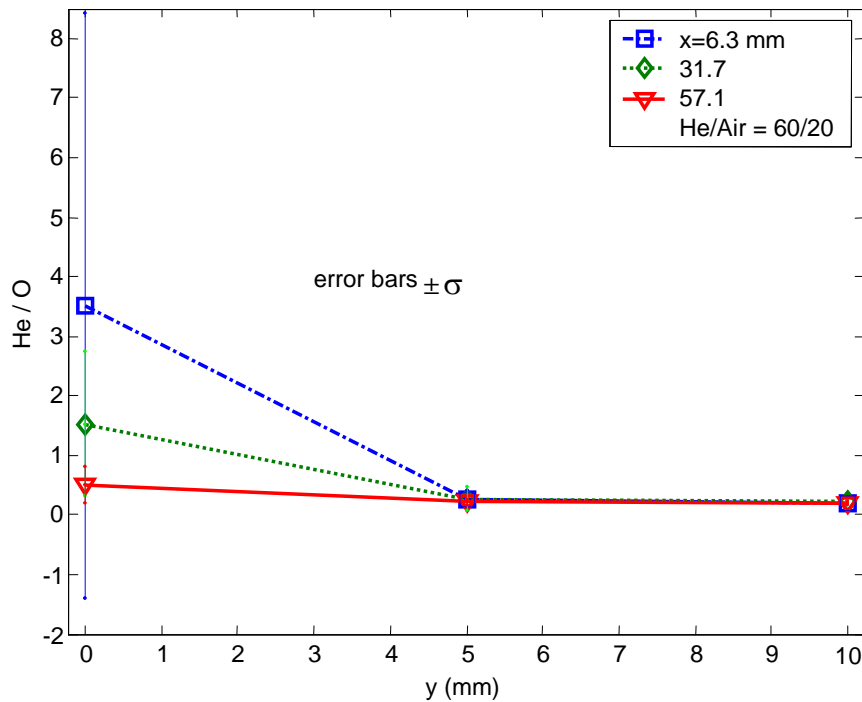


Figure 26 – He / O intensity ratio at the three downstream locations for the He/Air 60/20 case (w/cavity).

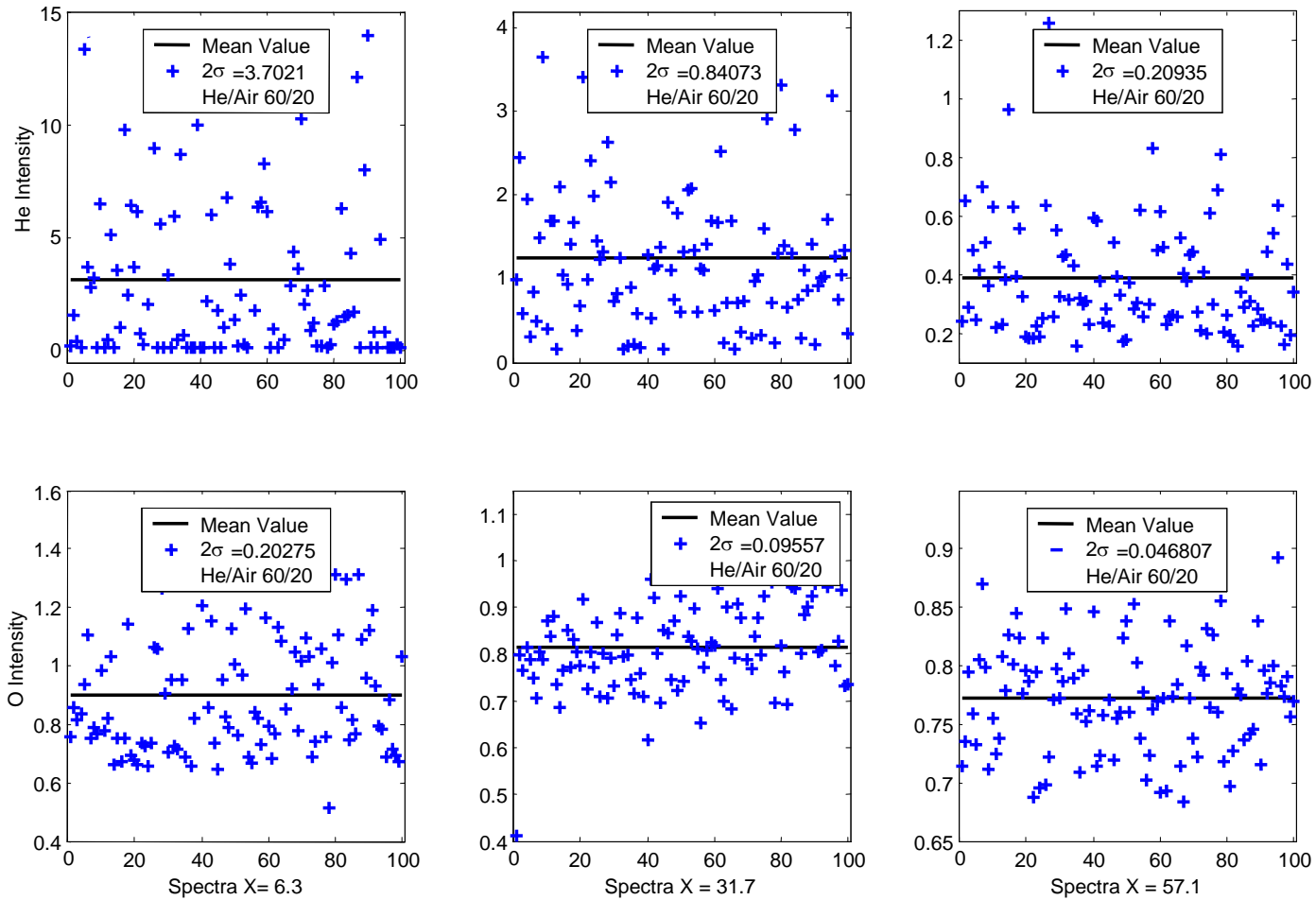


Figure 27 – Single-shot values of He and O intensities at $y = 0$ and $x = 6.3, 31.7,$ and 57.1 mm for the He/Air 60/20 pressure case (w cavity).

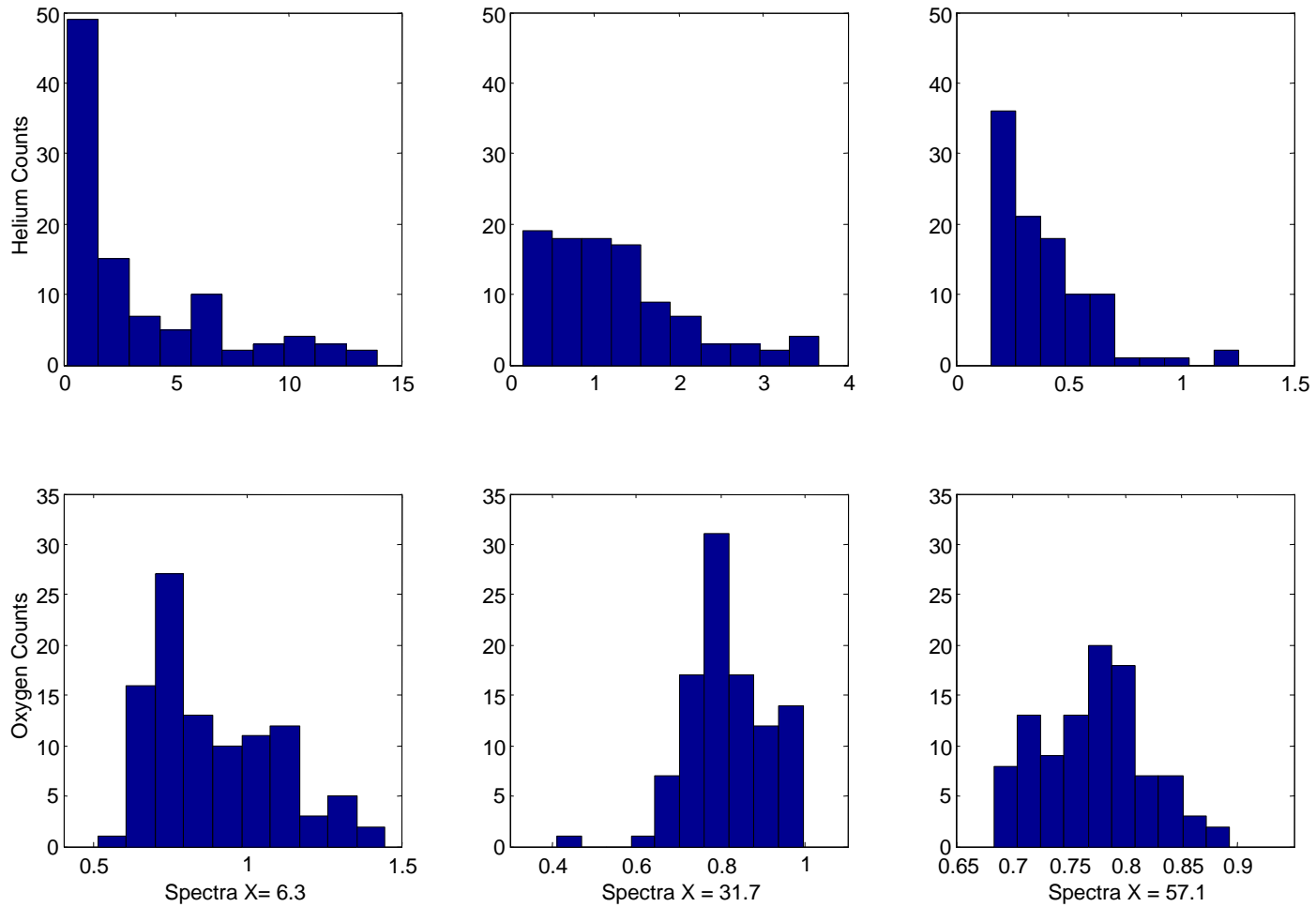


Figure 28 --Histograms of helium and oxygen intensity at $y = 0$ and $x = 6.3, 31.7,$ and 57.1 mm for the He/Air 60/20 pressure case (w/cavity).

Figure 29 and Figure 30 show the calculated percentage of helium at the nine measured locations for the He/Air 60/20 baseline and cavity case respectively. The measurement error was calculated using the sum of the fractional error of the oxygen and helium measurements plus the data fit fractional error. The O/He value was first used to determine the helium concentration, then the corresponding data fit fractional error value from that concentration was used to determine the total fractional error. The calculated helium percentage along with the total fractional error at each point is given in Table 1 and Table 2 for the baseline and cavity case respectively.

The graphs for additional pressure cases with and without a wall cavity are given in Appendix B – Graphs from Wind Tunnel Experiments. Figure 31 and Figure 32 show the difference between the He/O peak-to-base values when helium is 60 psi and air is 40 psi at $x = 6.3$ mm and $x = 56$ mm, with and without a cavity respectively. The results show that the average helium concentration is lower for the case with the cavity, as discussed above.

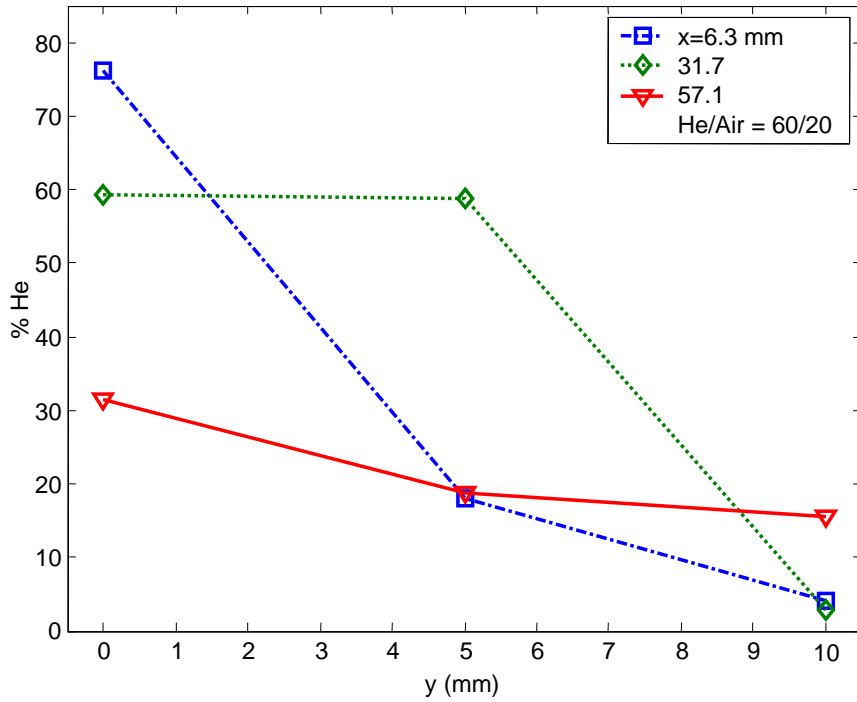


Figure 29 – Percent helium at the three downstream locations for the He/Air 60/20 pressure case (w/o cavity).

He / Air 60 / 40 w/o Cavity			
X	Y	% He	± % He
6.3	0	76	107
6.3	5	18	17
6.3	10	4.1	0.78
31.7	0	59	18
31.7	5	59	14
31.7	10	2.9	0.42
57.1	0	31	30
57.1	5	19	13
57.1	10	15	3.2

Table 1 – Calculated helium concentrations with error for the points shown in Figure 29.

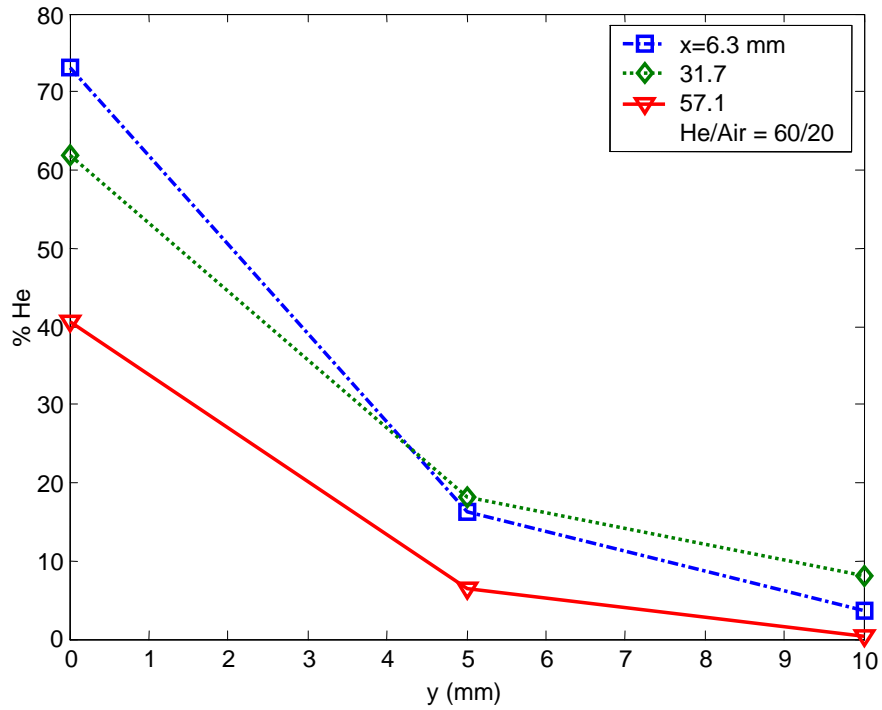


Figure 30 – Percent helium at the three downstream locations for the He/Air 60/20 pressure case (w/cavity).

He / Air 60 / 40			
X	Y	% He	± % He
6.3	0	73	220
6.3	5	16	23
6.3	10	3.6	0.83
31.7	0	62	110
31.7	5	18	33
31.7	10	8.1	2
57.1	0	40	55
57.1	5	6.4	2.5

Table 2 – Calculated helium concentrations with error for the points shown in Figure 30.

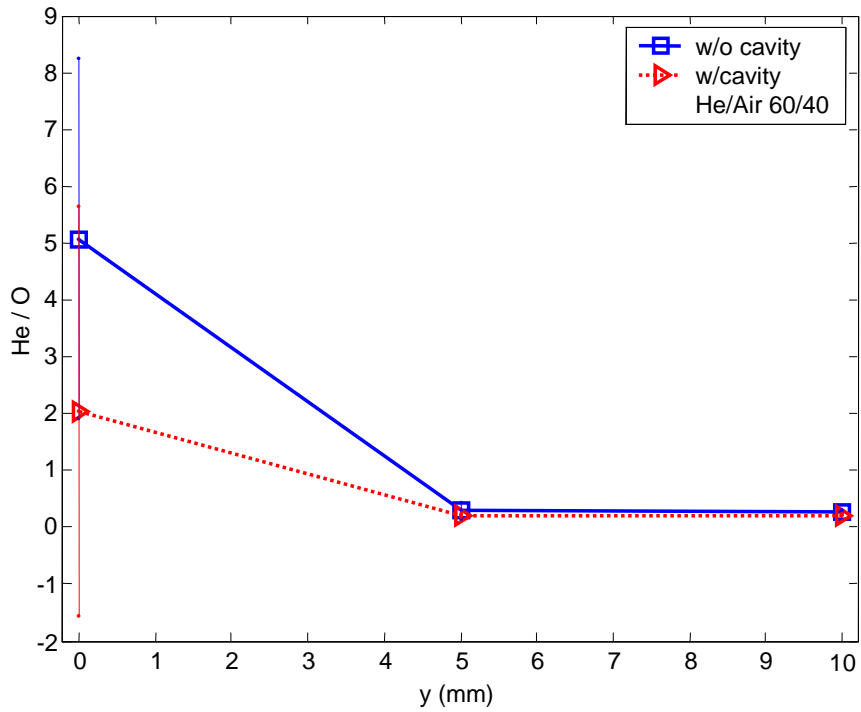


Figure 31 – He / O intensity at x=6.3 mm downstream for He/Air 60/40 psi.

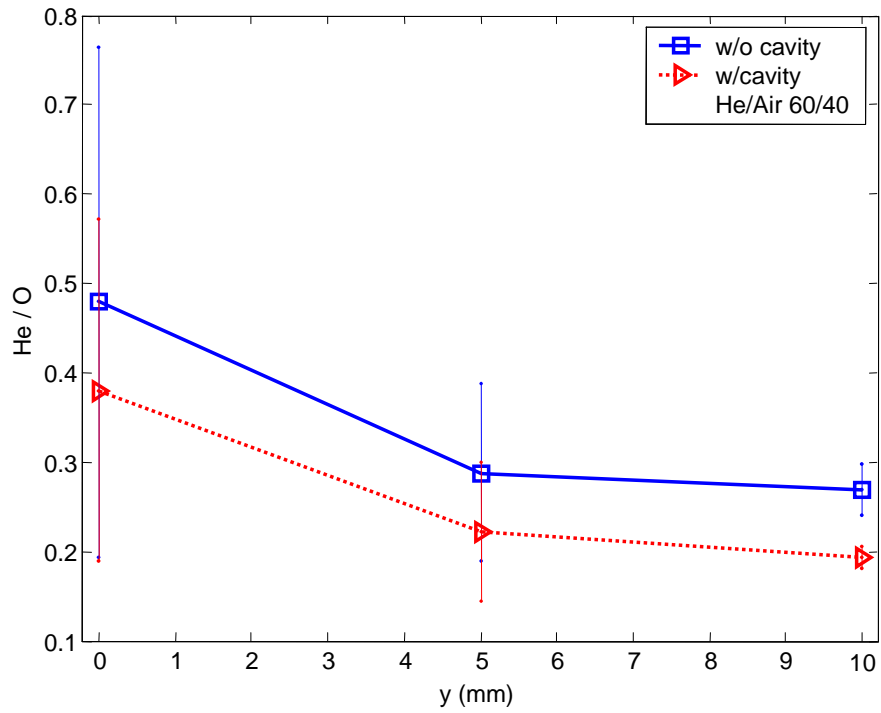


Figure 32 – He / O intensity at x=57.1 mm downstream for He/Air 60/40 psi.

4.4 Summary of Data

Laser-induced breakdown spectroscopy was used to measure helium concentrations in a supersonic wind tunnel. Experiments were done using three different sets of stagnation pressures for helium and air. Due to the limitations of the laser setup, measurements were only taken at one height above the bottom wall of the wind tunnel. The helium / oxygen intensity ratios show that the helium is the strongest directly downstream from where it is injected and that it diffuses toward the wall as it flows downstream.

Experiments using a wall cavity to enhance supersonic mixing were also completed. The data from both experiments fundamentally agree in the diffusion characteristics, but the mean helium/oxygen intensity levels were lower in the tests with the cavity. Because the same amount of helium was present in both experiments, this result indicates that in the test with the cavity, the helium mixed faster and was carried away from the sampled points, penetrating deeper into the supersonic flow. This matches the conclusions from past cavity enhanced supersonic mixing experiments that the helium becomes entrained in the vortices shed by the cavity and that the mixing rate is increased.

CHAPTER 5 ERROR ANALYSIS

5.1 Sources of Error

In any set of experiments it is important to understand and analyze the error present in the system. Generally, as the number of variables in an experiment increases, so do the number of possible sources of error. There are two main error sources in this set of experiments: the error inherent in the laser and collection optics setup and the error in determining the location of the spark. These errors were potentially compounded through the interchanging of components and the use of the laser and collection optics in other experiments during the same time period.

There are three possible major sources of error in the laser and the collecting optics setup. The variation in the laser power between shots and between experiments is the first. The second is the alignment of the beam expander, pierced mirror, and focusing lens. The final variable is the alignment of the collecting lens from the pierced mirror. The spectrometer and Winspec, the corresponding data collection program, are assumed to behave with a constant error throughout each experiment.

The shot-to-shot variation in laser power leads to an increase in the deviation of signal intensities between measurements. This deviation can lead to inconsistencies in the final, computed intensity values and increases the variance of signal intensity at any specific data point. The inter-experimental laser power could change significantly because between the experiments the laser was used by others for different purposes. The laser has a potentiometer, controlled by a coarsely adjustable knob, that is used to select the laser power and it is difficult return the power to the same level as in the

previous helium tests. The laser power was set between 70% and 80% of full power on the knob for each experiment, as noted below, more precise adjustment was not possible.

It was found that laser pulses at a higher frequency give larger signal intensities than lower frequency pulses due to the fact that the laser is optimized for high frequency (10 Hz) operation. During the diffusion jet experiments, measurements were taken at 10 Hz in the regions where the jets were mainly unmixed and turbulent fluctuations would not interfere with the experiments, i.e. directly above the helium jet or significantly into the free-stream air jet. Close to, or directly above the wall of the helium tube, where most mixing is expected to occur, single shot data was taken at approximately 0.5 Hz. More time was given between measurements to allow for the turbulence created by the prior spark to dissipate. No definite conclusions can be made concerning the relationship between the signal-to-noise ratio and the frequency of the laser pulses because detailed signal-to-noise ratio experiments at different laser operating frequencies were not done.

The second source of error, the alignment of the laser and delivering optics, was from the laser head being re-aligned for other experiments or from motion such as a bump to the measurement table. The position of the pierced mirror could change slightly between experiments as well. To compensate for this misalignment, a Coherent Lasermate-P power meter was used to measure the laser pulse after passing through the final focusing lens. The laser power knob, laser head location, and the pierced mirror were adjusted until the meter read between 3.75 and 4.25 W for each pulse. This value could not be identical for each experiment because of the difficulty in adjusting the coarse potentiometer controlling the laser power. This ensured a spark of relatively equal power in each experiment.

The collecting lens, which focuses on the reflective side of the pierced mirror, can become misaligned as well. This causes a significant decrease in the measured emission along the entire spectrum and significantly lowers the signal-to-noise ratio. To account for this possible loss of signal, the experiment was calibrated using the naturally occurring oxygen in the atmosphere. Before beginning any experiment and after any movement of the laser or optics setup, the oxygen and nitrogen intensities were measured. The collecting lens is adjusted until the oxygen intensity, averaged over 100 spectra, give a signal greater than 120,000 counts, but less than 150,000 counts.

The original calibration tests (Figure 9) were completed using the power range and collection optics settings described above. The agreement of the data from those experiments shows that the range of power between 3.75 and 4.25 W is valid. These results also indicate that the error caused by misalignment is small as long as the laser power and collecting optics meet the above requirements.

The error in spark location was only a factor in the diffusion tube and wind tunnel experiments. Throughout the original calibration experiment, the helium and air are completely pre-mixed prior to the jet exit so the spark is simply centered 2 mm's above the exit. During the annular tube experiment, the initial error in the location of the center of the spark is ± 0.25 mm. The tubes are mounted on two traversing stages that had an error of ± 0.05 mm and are required to move perpendicular to the optical setup. When the radially-traversing stage is translated 10 mm, the spark location was accurate within ± 0.5 mm giving an angular error of $\pm 18^\circ$. The large error in this angle measurement was considered acceptable because the radial distances measured rarely exceeded 10 mm so the error rarely exceeded ± 0.5 mm.

During the wind tunnel experiment, the setup was translated in both the x and y directions. The step size in the x direction is 25.4 mm because the breadboard used had a 25.4 ± 0.025 mm x 24.7 ± 0.025 mm grid of mounting holes. The y-location is set using one of the traversing stages from the annular jet experiment with ± 0.05 mm accuracy. The error in the original location of the spark is ± 0.5 mm in the x and y directions. The actual location of the spark could then be estimated within ± 0.525 mm in the x-direction and ± 0.530 mm in the y-direction.

The laser head, which rests on an aluminum platform above the breadboard table, also had to be shifted 25.4 mm downstream for different x positions. The breadboard grid was not available as a guide, so to properly align the laser head after each movement, markings were made on the supporting platform. The power output of the laser, alignment of the optics, and measurement of the oxygen intensity was recorded after each downstream movement. The oxygen intensity was measured as an accumulation of 100 spectra to ensure that the total would exceed 120,000 counts and as an additional measure, 100 individual spectra were recorded and averaged in Matlab. The oxygen peak-to-base values from each measurement at the three different x locations can be seen in Figure 33. Error bars shown are ± 1 standard deviation for the single-shot data and the figure shows the measurements agree well. These measurements assured that the laser and the corresponding optics were aligned similarly for each set of x measurements. The alignment error of the laser and collecting optics can effectively be neglected through monitoring the laser power, alignment, and oxygen intensity measurements.

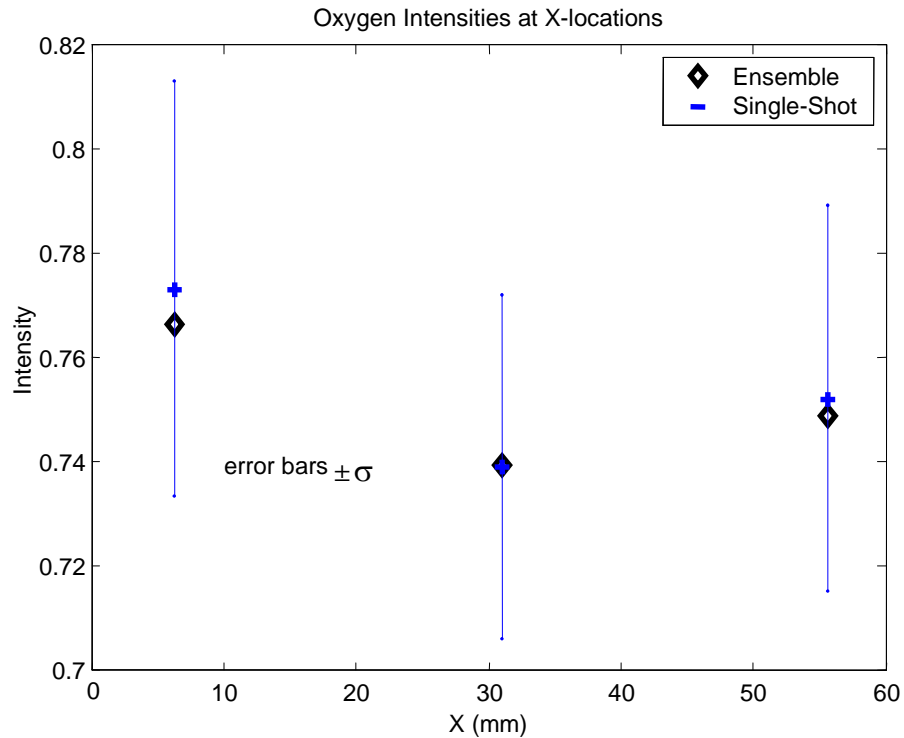


Figure 33 – Oxygen intensities measured during wind tunnel testing at downstream (X) locations.

5.2 Calculating Signal Intensity

As described in Section 2.1, there are two widely accepted methods to interpret the elemental line intensity, the Peak-to-Base (PB) and the Signal-to-Noise (SNR) ratio. Both ratios were calculated using the method described in Section 2.1 using the peak and featureless regions discussed in Section 3.2 and shown in Figure 3 and Figure 4. Previous experiments [9] have shown that the SNR is a more robust metric for analyte detection from single-shot measurements of aerosol particles. Both methods were used to determine helium and oxygen concentrations in the data fit and wind tunnel measurements. The values of fractional error in the data fit experiments for the PB and SNR methods are shown in Table 3. The right-most column is the percentage increase in fractional error between the PB and SNR methods. The PB method is shown to give

smaller fractional errors and is thus considered the better metric for concentration measurements of a gas mixture.

Fractional Errors PB vs. SNR							
% He	O (PB)	O (SNR)	He (PB)	He (SNR)	Total (PB)	Total (SNR)	Δ %
0.0	0.0143	0.045	0.0018	0.016	0.0161	0.061	278.9
4.9	0.0052	0.0198	0.0038	0.0092	0.009	0.029	222.2
9.3	0.0165	0.0148	0.0036	0.0159	0.0201	0.0307	52.7
15.9	0.0047	0.1014	0.0064	0.0214	0.0111	0.1228	1006.3
21.5	0.0132	0.1152	0.0286	0.0279	0.0418	0.1431	242.3
29.1	0.0096	0.0426	0.0196	0.0055	0.0292	0.0481	64.7
36.8	0.0191	0.08	0.0528	0.0414	0.0719	0.1214	68.8
41.6	0.0188	0.0846	0.0217	0.0104	0.0405	0.095	134.6
45.8	0.0304	0.0709	0.0935	0.0659	0.1239	0.1368	10.4
49.6	0.0063	0.0516	0.0579	0.0468	0.0642	0.0984	53.3
54.6	0.0261	0.0566	0.1166	0.1231	0.1427	0.1797	25.9
59.6	0.0115	0.0758	0.1151	0.0996	0.1266	0.1754	38.5
65.2	0.009	0.0871	0.0967	0.0835	0.1057	0.1706	61.4
70.5	0.0109	0.05	0.0777	0.0687	0.0886	0.1187	34.0
75.4	0.0249	0.0567	0.2991	0.2175	0.324	0.2742	-15.4
79.1	0.0148	0.082	0.1139	0.0799	0.1287	0.1619	25.8
82.9	0.0125	0.054	0.199	0.1492	0.2115	0.2032	-3.9
99.8	0.0112	0.1112	0.0473	0.0272	0.0585	0.1384	136.6

Table 3 – Fractional error in oxygen and helium intensity using PB and SNR during data fit experiment.

The PB ratio is expected to have smaller fractional errors for both the data fit and the annular tube experiment because the measurements in both of these experiments are ensemble-averaged to reduce the random noise, as noted in Section 2.1. The measurements in the wind tunnel are single-shot spectra, allowing a more accurate comparison of the error present in both methods.

A direct comparison of the O/He intensities and the helium concentration values between the two methods can not be made because the data fit from Figure 9 is calculated using PB intensity. The fractional error in each measurement can be determined from the

experimental data. In Table 4 Table 9, the oxygen and helium fractional error is shown, along with the total error percentage increase, between the PB and SNR methods. Table 4, Table 5, and Table 6 contain the baseline data, while Table 7, Table 8, and Table 9 display the data using the cavity. At almost every measurement point, the PB method has a smaller fractional error than the SNR.

Fractional Error Comparison				
He / Air 40 / 20 w/o Cavity				
X (mm)	Y (mm)	P/B	SNR	% Change
6.3	0	1.8	1.6	-11.1
6.3	5	1.1	1.24	12.7
6.3	10	0.24	0.54	125.0
31.7	0	2.2	2	-9.1
31.7	5	0.21	0.72	242.9
31.7	10	0.12	0.91	658.3
57.1	0	1.5	1.6	6.7
57.1	5	0.14	0.27	92.9
57.1	10	0.21	0.44	109.5

Table 4 – Values of total fractional error when using PB and SNR methods (40/20 case w/o cavity).

Fractional Error Comparison				
He / Air 60 / 20 w/o Cavity				
X (mm)	Y (mm)	P/B	SNR	% Change
6.3	0	1.4	1.26	-10.0
6.3	5	0.91	0.99	8.8
6.3	10	0.18	0.47	161.1
31.7	0	0.28	0.97	246.4
31.7	5	0.22	0.81	268.2
31.7	10	0.14	0.41	192.9
57.1	0	0.95	1	5.3
57.1	5	0.67	0.85	26.9
57.1	10	0.2	0.45	125.0

Table 5 – Values of total fractional error when using PB and SNR methods (60/20 case w/o cavity).

Fractional Error Comparison				
He / Air 60 / 40 w/o Cavity				
X (mm)	Y (mm)	P/B	SNR	% Change
6.3	0	1.2	1.2	0.0
6.3	5	1	1.2	20.0
6.3	10	0.2	0.46	130.0
31.7	0	0.23	0.91	295.7
31.7	5	0.16	0.6	275.0
31.7	10	0.12	0.39	225.0
57.1	0	1.2	1.3	8.3
57.1	5	0.67	0.89	32.8

Table 6 – Values of total fractional error when using PB and SNR methods (60/40 case w/o cavity).

Fractional Error Comparison				
He / Air 40 / 20 with Cavity				
X (mm)	Y (mm)	P/B	SNR	% Change
6.3	0	4.6	4.3	-6.5
6.3	5	0.18	0.45	150.0
6.3	10	0.14	0.88	528.6
31.7	0	2.1	1.9	-9.5
31.7	5	0.62	1.3	109.7
31.7	10	0.21	0.59	181.0
57.1	0	1.7	1.9	11.8
57.1	5	0.77	0.69	-10.4
57.1	10	0.13	0.41	215.4

Table 7 – Values of total fractional error when using PB and SNR methods (40/20 case with cavity).

Fractional Error Comparison				
He / Air 60 / 20 with Cavity				
X (mm)	Y (mm)	P/B	SNR	% Change
6.3	0	2.8	2.56	-8.6
6.3	5	1.4	1.52	8.6
6.3	10	0.18	0.49	172.2
31.7	0	1.6	2	25.0
31.7	5	1.5	1.3	-13.3
31.7	10	0.19	1.1	478.9
57.1	0	1.2	1.1	-8.3
57.1	5	0.34	0.9	164.7
57.1	10	0.21	0.58	176.2

Table 8 – Values of total fractional error when using PB and SNR methods (60/20 case with cavity).

Fractional Error Comparison				
He / Air 60 / 40 with Cavity				
X (mm)	Y (mm)	P/B	SNR	% Change
6.3	0	3.5	3.6	2.9
6.3	5	0.33	0.52	57.6
6.3	10	0.14	0.79	464.3
31.7	0	1.6	1.5	-6.3
31.7	5	1	1	0.0
31.7	10	0.15	1.2	700.0
57.1	0	1	1	0.0
57.1	5	0.71	0.76	7.0
57.1	10	0.13	0.44	238.5

Table 9 – Values of total fractional error when using PB and SNR methods (60/40 case with cavity).

CHAPTER 6 CONCLUSIONS

Laser induced breakdown spectroscopy is a viable option for measuring local elemental concentration levels in a supersonic wind tunnel. Non-reacting flow using helium to simulate hydrogen was tested in a supersonic wind tunnel at University of Maryland, College Park. Experiments were performed using three different sets of helium and air gauge pressures both with and without a wall cavity.

Previous experiments have shown that a wall cavity can produce coherent structures in supersonic flow which increase the shear layer growth rate. These experiments show that the helium was entrained in the large, coherent structures shed by the cavity. This entrainment caused the helium to penetrate further into the supersonic flow and to mix away from the bottom wall of the wind tunnel. More detailed experiments with measurements at various heights would be beneficial to understanding the helium / air distribution under various operating conditions.

The data obtained from LIBS at specific points in the flow can be used to determine local gas mixing ratios. LIBS is an attractive supersonic diagnostic tool because it is non-invasive, requiring only optical access to the flow. These measurements can quantify and compare different methods of supersonic mixing enhancement and be used to validate numerical simulations of supersonic flow. LIBS can also be applied to supersonic reacting flow because of its ability to measure both the products and reactants of the combustion process.

The PB and SNR methods are used to determine the elemental line intensities for each experiment. The PB method is shown to produce a smaller fractional error in the helium and oxygen intensity measurements. Thus the PB method is a better metric for calculating elemental line intensity in a gas mixture.

Laser-induced breakdown spectroscopy has also been shown to have the capability to accurately measure up to 75% volumetric helium with conservatively-determined (2σ -based) fractional errors of $\pm 5\%$, $\pm 15\%$, $\pm 25\%$, and $\pm 45\%$ in ranges of 0-25%, 25%-45%, and 45%-75%, and 75-100% helium respectively. The process described in this paper that is used to determine the sensitivity limits for helium can be extended to a range of gases. For future experiments, fuels such as propane or hydrogen could potentially be used with little or no modification to the existing setup.

REFERENCES

- [1] Bonnet, J. P., Gresillon, D., and Taran, J.P., “Nonintrusive Measurements for High-Speed, Supersonic, and Hypersonic Flows,” *Annual Review of Fluid Mechanics*, Vol. 30, 231-273, 1998.
- [2] Hanafi, M., Omar, M.M., and Gamal, Y.E.E-D., “Study of Laser-Induced Breakdown Spectroscopy of Gases,” *Radiation Physics and Chemistry*, Vol. 57, 11-20, 2000.
- [3] Hahn, D.W., Flower, W.L., and Hencken, K.R., “Discrete Particle Detection and Metal Emissions Monitoring Using Laser-Induced Breakdown Spectroscopy,” *Applied Spectroscopy*, Vol. 51, Number 12, 1997.
- [4] Carranza, J.E. and Hahn, D.W., “Sampling Statistics and Considerations for Single-Shot Analysis Using Laser-Induced Breakdown Spectroscopy,” *Spectrochimica Acta Part B*, Vol. 57, 779-790, 2002.
- [5] Buckley, S. G., Johnsen, H. A., Hencken, K. R., and Hahn, D. W., “Implementation of Laser-Induced Breakdown Spectroscopy as a Continuous Emissions Monitor for Toxic Metals,” *Waste Management*, Volume 20, 455-462, 2000.
- [6] Ferioli, F., Puzinauskas, P. V., and Buckley, S. G., “Laser-Induced Breakdown Spectroscopy for Real-Time Engine Equivalence Ratio Measurements,” *Applied Spectroscopy*, Vol. 57, No. 9, 1183-1189, 2003.
- [7] Ferioli, F. and Buckley, S. G., “Measurements of Hydrocarbons using Laser-Induced Breakdown Spectroscopy,” *Combustion and Flame*, to be submitted.
- [8] Radziemski, L. J., “From LASER to LIBS, the path of Technology Development,” *Spectrochimica Acta Part B*, Volume 57, 1109-1113, 2002.

- [9] Carranza, J. E., Iida, K., and Hahn, D. W., "Conditional data processing for single-shot spectral analysis by use of laser-induced breakdown spectroscopy," *Applied Optics*, Vol. 42, No. 30, 2003.
- [10] Detalle, V., Sabsabi, M., St-Onge, L., Hamel, A. and Heon, R., "Influence of Er:YAG and Nd:YAG Wavelengths on Laser-Induced Breakdown Spectroscopy Measurements under Air or Helium Atmosphere," *Applied Optics*, Vol. 42, No. 30, 2003.
- [11] Yu, K. and Schadow, K.C., "Cavity-Actuated Supersonic Mixing and Combustion Control," *Combustion and Flame*, Vol. 99, 295-301, 1994.
- [12] Yu, K. and Schadow, K.C., "Role of Large Coherent Structures in Turbulent Compressible Mixing," *Experimental Thermal and Fluid Science*, Vol. 14, 17-84, 1997.
- [13] Yu, K., Wilson, K.J., Smith, R.A., and Schadow, K.C., "Experimental Investigation on Dual-Purpose Cavity in Supersonic Reacting Flows," AIAA 98-0723.
- [14] Yu, K., Wilson, K.J., and Schadow, K.C., "Effect of Flame-Holding Cavities on Supersonic-Combustor Performance," *Journal of Propulsion and Power*, Vol. 17, No. 6, 2001.
- [15] Gutmark, E.J., Schadow, K.C., Yu, K., "Mixing Enhancement in Supersonic Free Shear Flows," *Annual Review of Fluid Mechanics*, Vol. 27, 375-417, 1995.
- [16] Tishkoff, J.M., Drummond, J.P, Edwards, T., and Nejad, A.S., "Future Directions of Supersonic Combustion Research – Air Force/NASA Workshop on Supersonic Combustion," AIAA, Aerospace Sciences Meeting & Exhibit, 35th, 1997.

- [17] Song, K, Lee, Y.-I., and Sneddon, J., "Recent Developments in Instrumentation for Laser Induced Breakdown Spectroscopy." *Applied Spectroscopy Reviews* 37(1), 89-117, 2002.
- [18] Cutler, A.D. and Diskin, G.S., "Fundamental Mixing and Combustion Experiments for Propelled Hypersonic Flight," *AIAA*, 38th AIAA/ASME/SAE/ASEE Joint Propulsion Conference and Exhibit, 2002-3879.
- [19] Baurle, R.A., Gruber, M.R., "A Study of Recessed Cavity Flowfields for Supersonic Combustion Applications," *AIAA 98-0938*, 36th Aerospace Sciences Meeting & Exhibit, 1998.
- [20] Burnes, R., Parr, T.P., and Yu, K., "Investigation of Supersonic Mixing Control Using Cavities: Effect of Fuel Injection Location," *AIAA 2000-3618*.
- [21] Yang, S.R., Zhao, J.R., Sung, C.J., Yu, G., "Multiplex CARS Measurements in Supersonic H₂/air Combustion," *Applied Physics B Lasers and Optics*, Vol. 68, 257-265, 1999.
- [22] Dudragne, L., Adam, P., and Amouroux, J., "Time-Resolved Laser-Induced Breakdown Spectroscopy: Application for Qualitative and Quantitative Detection of Fluorine, Chlorine, Sulfur, and Carbon in Air," *Applied Spectroscopy*, Vol. 52, No. 10, 1998.
- [23] Rusak, D.A., Castle, B.C., Smith, B.W., Winefordner, J.D., "Recent Trends and the Future of Laser-Induced Plasma Spectroscopy," *Trends in Analytical Chemistry*, vol. 17, No. 8+9, 1998.

- [24] Zhao, F-Q. and Hiroyasu, H., "The Applications of Laser Rayleigh Scattering to Combustion Diagnostics," *Progress in Energy and Combustion Science*, Vol. 19, 447-485, 1993.
- [25] Applied Combustion Diagnostics, *Combustion: An International Series*, edited by Kohse-Hoinghaus, K. and Jeffries, J. B., Taylor & Francis, New York, NY, 2002.
- [26] Sneddon, J and Lee, Yong-III, "Novel and Recent Applications of Elemental Determination by Laser-Induced Breakdown Spectrometry," *Analytical Letters*, 32 (11), 2143-2162, 1999.
- [27] Phuoc, T. X. and White, C. M., "Experimental Studies of the Absorption and Emission from Laser-Induced Spark in Combustible Gases," *Optics Communication*, Vol. 181, 353-359, 2000.
- [28] Phuoc, T. X. and White, F. P., "Laser-Induced Spark for Measurements of the Fuel-to-Air Ratio of a Combustible Mixture," *Fuel*, Vol. 81, 1761-1765, 2002.
- [29] Nenmeni, V. A. R., "Flow Induced Cavity Resonance for Turbulent Compressible Mixing Enhancement in Scramjets," *Master's Thesis*, Univ. of MD, College Park, 2002.
- [30] Brown, G.L., and Roshko, A., "On Density Effects and Large Structure in Turbulent Mixing Layers," *Journal of Fluid Mechanics*, Vol. 64, Pt. 4, 1974, pp. 775-816.
- [31] Papamouschou, D., and Roshko, A., "The Compressible Turbulent Shear Layer: An Experimental Study," *Journal of Fluid Mechanics*, Vol. 197, 1988, pp. 453-477.

- [32] Seiner, J.M., Dash, S.M., and Kenzakowski, D.C., "Historical Survey on Enhanced Mixing in Scramjet Engines," *Journal of Propulsion and Power*, Vol. 17, No. 6, 2001, pp. 1273-1286.
- [33] Dyer, T. M., "Rayleigh Scattering Measurements of Time-Resolved Concentration in a Turbulent Propane Jet," *AIAA Journal*, Vol. 17, 912-914, August 1979.
- [34] Fisher, B. T., Johnsen, H., Buckley, S., and Hahn, D. W., "Temporal Gating for the Optimization of Laser-Induced Breakdown Spectroscopy Detection and Analysis of Toxic Metals," *Applied Spectroscopy*, Vol. 55, No. 10, 2001.
- [35] Carranza, J.E. and Hahn, D. W., "Plasma Volume Considerations for Analysis of Gaseous and Aerosol Samples Using Laser-Induced Breakdown Spectroscopy," *Journal of Analytical Atomic Spectrometry*, Vol. 17., 1534-1539, 2002.
- [36] Radziemski, L.J., Loree, T.R., Cremers, D.A., and Hoffman, N.M., "Time-Resolved Laser-Induced Spectrometry of Aerosols," *Analytical Chemistry*, Vol. 55, 1246-1252, 1983.
- [37] Schechter, I., "Direct Aerosol Analysis by Time Resolved Laser Plasma Spectroscopy – Improvement by Single Shot Measurements," *Analytical Science and Technology*, Vol. 8, 779, 1995.

APPENDIX A – GRAPHS FROM COAXIAL JET EXPERIMENT

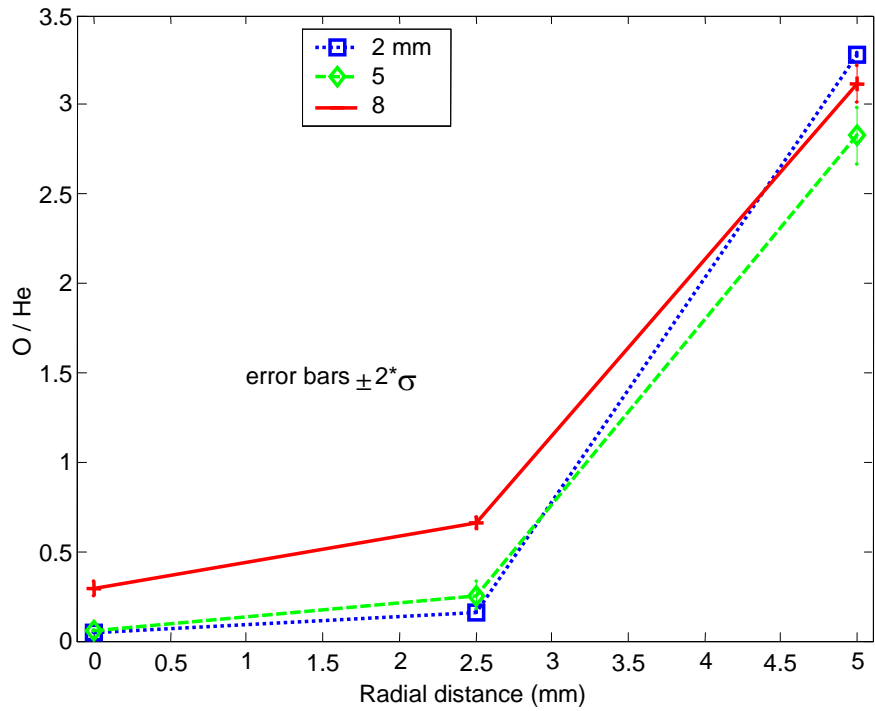


Figure 34 – He / O Ratio at various heights from February 2nd.

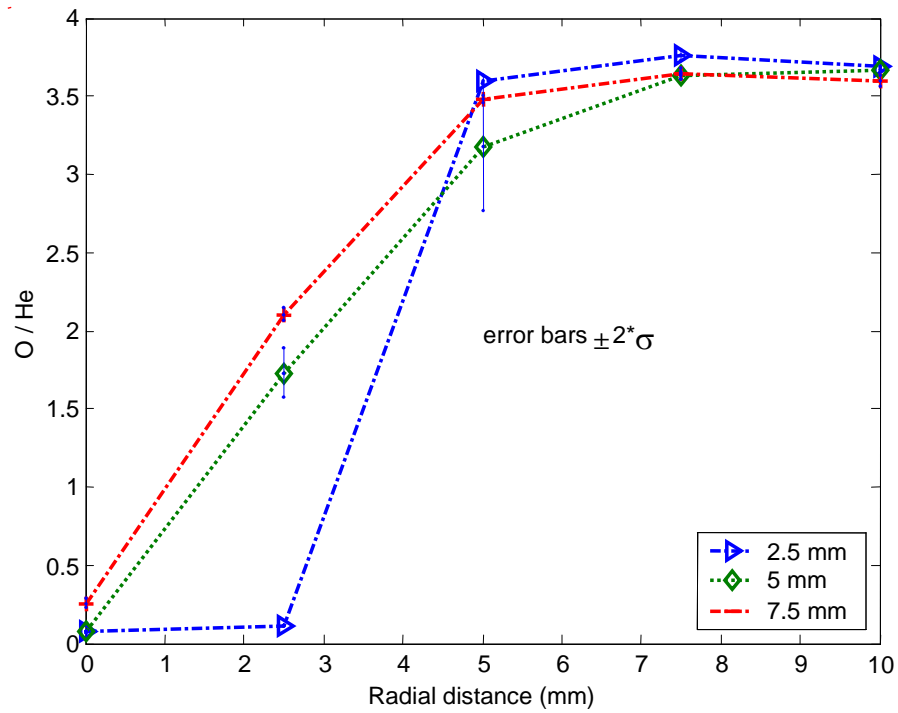


Figure 35 – He / O Ratio at various heights from February 3rd.

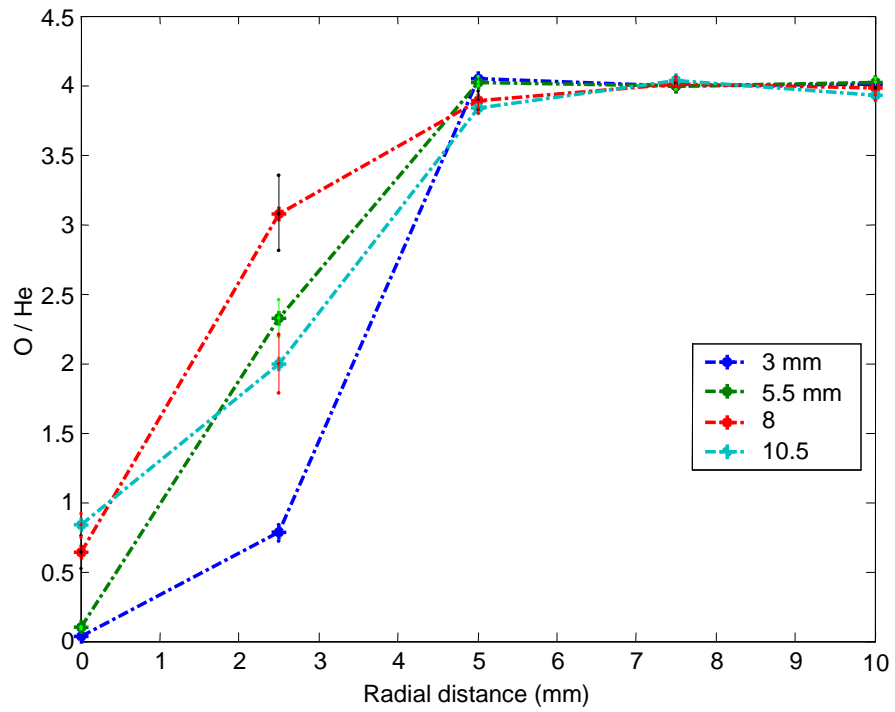


Figure 36 – He / O Ratio at various heights from February 3rd (b).

APPENDIX B – GRAPHS FROM WIND TUNNEL EXPERIMENTS

I Baseline – No Cavity

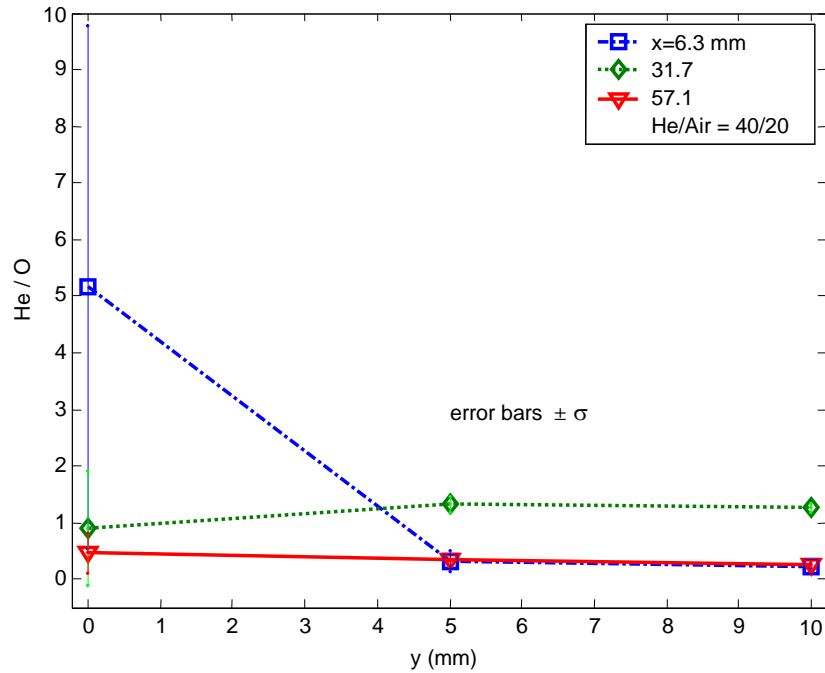


Figure 37 – He / O Ratio at each point for the Air/He 20/40 psi case without the cavity.

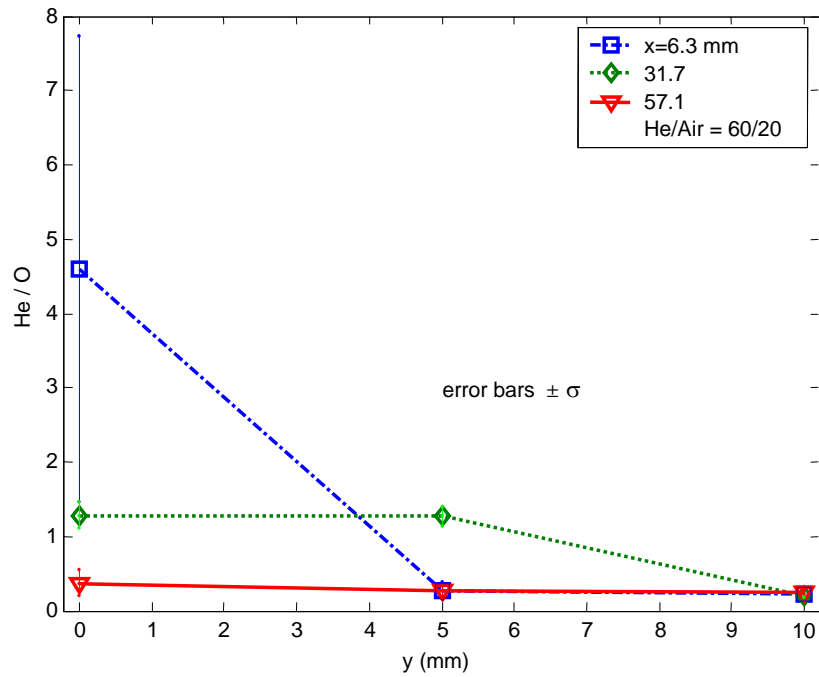


Figure 38 – He / O Ratio at each point for the Air/He 20/60 psi case without the cavity.

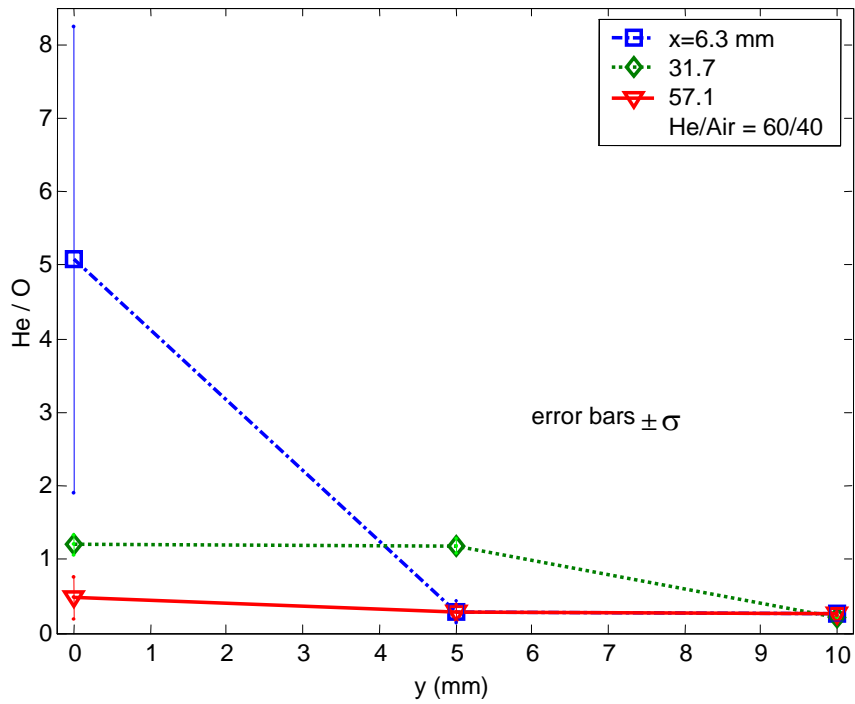


Figure 39 – He / O Ratio at each point for the Air/He 40/60 psi case without the cavity.

II With Cavity

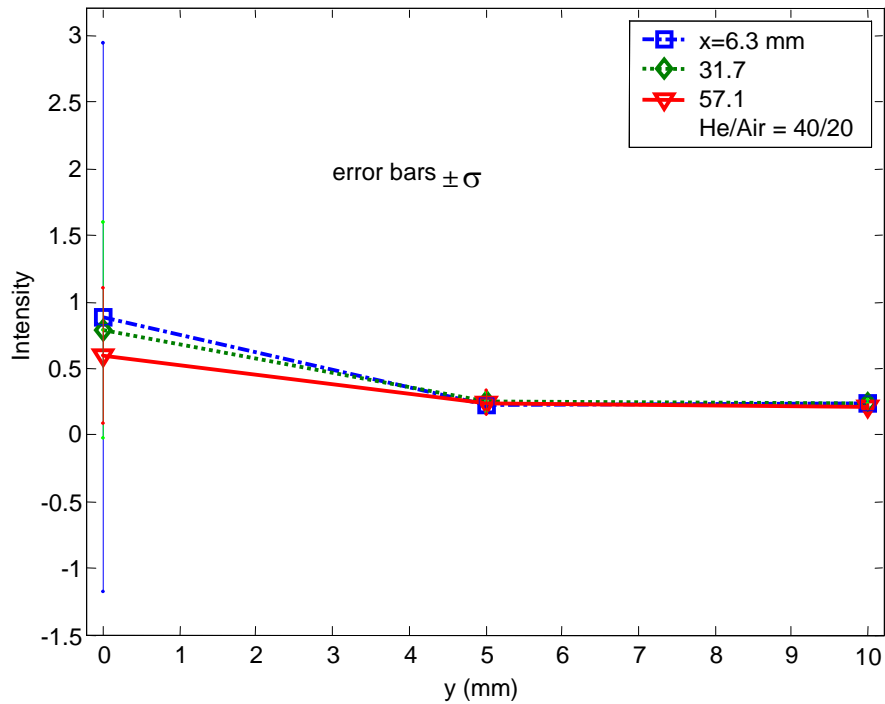


Figure 40 – He / O Ratio at each point for the Air/He 20/40 psi case with the cavity.

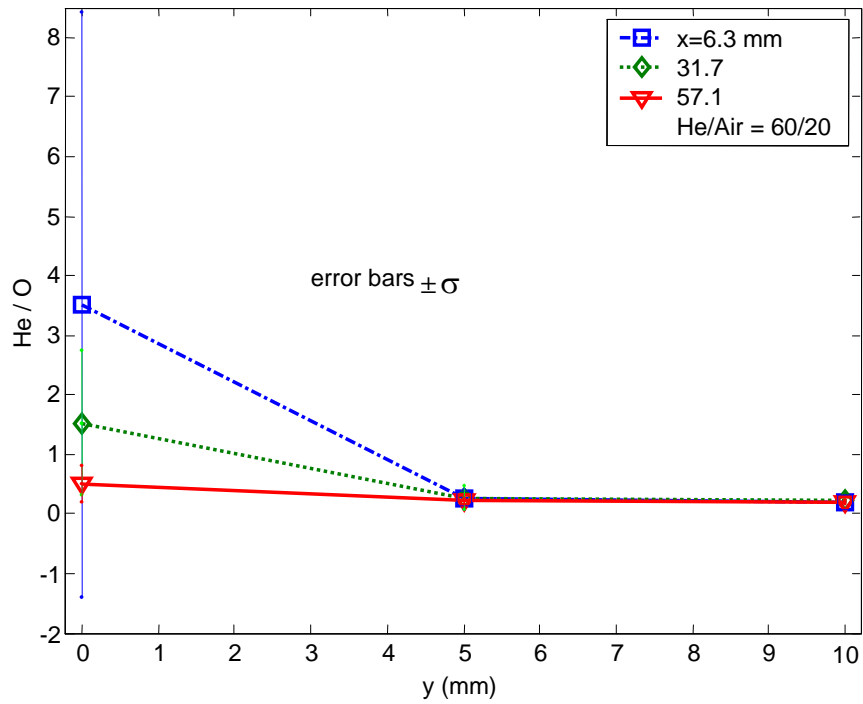


Figure 41 – He / O Ratio at each point for the Air/He 20/60 psi case with the cavity.

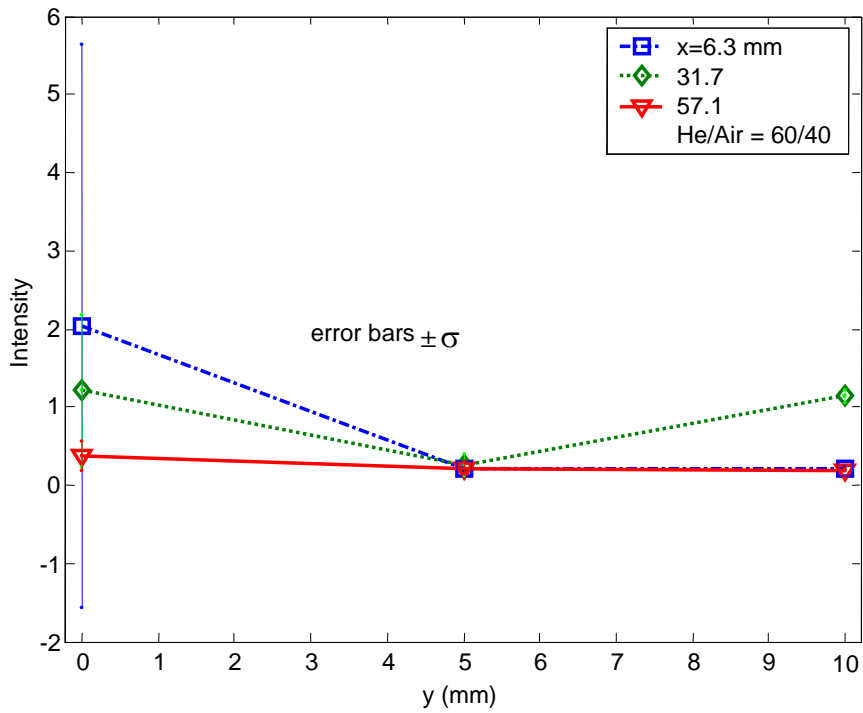


Figure 42 – He / O Ratio at each point for the Air/He 40/60 psi case with the cavity.

APPENDIX C – MATLAB M-FILES

I Signal Characterization

```
%% Data importation and division by base value

clc; clear; close all;
a=1:1024; b=1025:2048; c=2049:3072;
air3=2.091; helium3=[0 .1070 .2147 .3953 .5726 .8564 1.216 1.491 1.768 2.054 2.512 3.084 3.909 4.989...
    6.408 7.915 10.16 1000];
he3=100*helium3./(helium3+air3);
he_tot=[he3]; he115b=he_tot; save he115b he115b
for i=1:18
    o(:,i)=dlmread(['exptests\1_15b\O_255gain_100shots_', num2str(i), '.txt'], ' ', 0, 3);
    h(:,i)=dlmread(['exptests\1_15b\he_255gain_100shots_', num2str(i), '.txt'], ' ', 0, 3);
end
for j=1:18
    o(a,j)=o(a,j)/(sum(o(325:425,j))); o(b,j)=o(b,j)/(sum(o(1349:1449,j)));
    o(c,j)=o(c,j)/(sum(o(2373:2473,j)));
    h(a,j)=h(a,j)/(sum(h(200:300,j))); h(b,j)=h(b,j)/(sum(h(1424:1524,j)));
    h(c,j)=h(c,j)/(sum(h(2248:2348,j)));
end

%% Calculation of average signal intensity and O/he ratio

%% N1 744.8-757.45 x(511:532) O 773-777.86 x(736:775)
N1=[sum(o(511:532,:)); sum(o(1535:1556,:)); sum(o(2559:2580,:))]; N1=sum(N1);
O=[sum(o(736:775,:)); sum(o(1760:1799,:)); sum(o(2784:2823,:))]; O=sum(O);
he=[sum(h(490:512,:)); sum(h(1514:1536,:)); sum(h(2538:2560,:))]; he=sum(he);
ratio115b=O./he; save ratio115b ratio115b
he_sum115b=he; save he_sum115b he_sum115b
O_sum115b=O; save O_sum115b O_sum115b

%% Graphical representation of results

figure; plot(he_tot,[N1; O], '*-'); xlabel('% Helium'); ylabel('Intensity');
title('O N Intensity vs. Helium Concentration'); legend('N', 'O');
figure; plot(he_tot,[he], '*-'); xlabel('% Helium'); ylabel('Intensity');
title('He Intensity vs. Helium Concentration');
figure; plot(he_tot, ratio115b, '*-'); title('Jan. 15 Oxygen Signal/ Helium Signal');
xlabel('% Helium'); ylabel('O/He')
```

II Annular Tube Experiment

```
%%% Data Importation and division by base value
```

```
clc; clear; close all
x=[0 2.5 5]; power= repmat(2.85,1,24); a=1:1024; b=1025:2048; c=2049:3072;
for i=1:24
    y(:,i)=dlmread(['exptests\2_02\he150_o255_',num2str(i),'.txt'],' ', 0, 3)/power(i);
end
o_index=[2 3 6 11 10 7 14 15 18 23 22 19]; o=y(:,o_index);
h_index=[1 4 5 12 9 8 13 16 17 24 21 20]; h=y(:,h_index);
for j=1:12
    o(a,j)=o(a,j)/(sum(o(325:425,j))); o(b,j)=o(b,j)/(sum(o(1349:1449,j)));
    o(c,j)=o(c,j)/(sum(o(2373:2473,j)));
    h(a,j)=h(a,j)/(sum(h(200:300,j))); h(b,j)=h(b,j)/(sum(h(1424:1524,j)));
    h(c,j)=h(c,j)/(sum(h(2248:2348,j)));
end
```

```
%%% Calculation of Signal Intensity and O / He ratio
```

```
O=[sum(o(736:775,:)); sum(o(1760:1799,:)); sum(o(2784:2823,:))]; O=sum(O);
Oa=O(1:3); Ob=O(4:6); Oc=O(7:9); Od=O(10:12);
he=[sum(h(490:512,:)); sum(h(1514:1536,:)); sum(h(2538:2560,:))]; he=sum(he);
hea=he(1:3); heb=he(4:6); hec=he(7:9); hed=he(10:12);
ratioa=Oa./hea; ratiob=Ob./heb; ratioc=Oc./hec; ratiod=Od./hed;
ratio2_02=[ratioa; ratiob;ratioc;ratiod]; save ratio2_02 ratio2_02
he2_02=[hea; heb; hec; hed]; x2_02=x;
save x2_02 x2_02
```

```
%%% Visualization of results
```

```
figure; plot(x,[hea; heb; hec; hed], '*-'); legend('2 mm', '5 mm', '8 mm', '11 mm', 0); xlabel('radial distance (mm)'); ylabel('Intensity'); title('Helium 2/2/04');
figure; plot(x,[ratioa; ratiob; ratioc; ratiod], '*-'); legend('2 mm', '5 mm', '8', '11', 0); xlabel('radial distance (mm)'); ylabel('Ratio');
title('O / He vs. radial distance from centerline 2/2');
```

III Wind Tunnel Experiments

```
%%% Data Importation

clc; clear; close all;
%%% loads all files
for i=1:54
    y(:,i)=dlmread(['exptests\windtunnel\3_20\tunneltest_3_20_',num2str(i),'.txt'],' ', 0, 3);
end

%%% separates into helium or oxygen spectra
h=y(:,[2 3 6 7 10 11 14 15 18 19 22 23 26 27 30 31 34 36 38 39 42 43 46 47 50 51 54]);
o=y(:,[1 4 5 8 9 12 13 16 17 20 21 24 25 28 29 32 33 35 37 40 41 44 45 48 49 52 53]);

%%% normalizes the 100 spectra in each file with respect to background power
for j=1:size(o,2)
    for jj=1:100
        a=1024*jj-1023; b=1024*jj;
        o(a:b,j)=o(a:b,j)/(sum(o(324+a:424+a,j)));
        h(a:b,j)=h(a:b,j)/(sum(h(199+a:299+a,j)));
    end
end

%%% CALCULATION OF SIGNAL INTENSITIES

%%% calculates the average helium and oxygen signals for 100 spectra in each file
for k=1:size(o,2)
    for kk=1:100
        a=1024*kk-1023;
        O(kk,k)=sum(o(735+a:774+a,k));
        He(kk,k)=sum(h(489+a:511+a,k));
    end
end
O3_20=O; He3_20=He;
save WT_3_20 O3_20 He3_20

O=O3_20; He=He3_20; %%% Averages
O_avg=mean(O); He_avg=mean(He); Ratio=He_avg./O_avg;
ind_1=[27 22 21; 10 15 16; 9 4 3]; %%% Air 20 He 40 psi 0; 5; 10 mm
ind_2=[26 23 20; 11 14 17; 8 5 2]; %%% Air 20 He 60
ind_3=[25 24 19; 12 13 18; 7 6 1]; %%% Air 40 He 60
O_avg1=O_avg(ind_1); O_avg2=O_avg(ind_2); O_avg3=O_avg(ind_3);
He_avg1=He_avg(ind_1); He_avg2=He_avg(ind_2); He_avg3=He_avg(ind_3);
Ratio1=Ratio(ind_1); Ratio2=Ratio(ind_2); Ratio3=Ratio(ind_3);

%%% VISUALIZATION OF RESULTS

x=[0 5 10];
%%% Ratio Intensity Plots for each case
figure; plot(x,Ratio1,'*-'); xlabel('y (mm)'); ylabel('Intensity');
title('He / O vs. Y Air = 20 psi He = 40'); legend('x=6 mm','31','56');
figure; plot(x,Ratio2,'*-'); xlabel('y (mm)'); ylabel('Intensity');
legend('x = 6 mm','31','56'); title('He / O vs. Y Air = 20 psi He = 60');
figure; plot(x,Ratio3,'*-'); xlabel('y (mm)'); ylabel('Intensity');
```

```

legend('x = 6 mm','31','56'); title('He / O vs. Y Air = 40 psi He = 60')

%%% VISUALIZATION (continued)

%%% Ratio Intensity for each case at x= 6, 31, 56 mm
figure; plot(x,Ratio1(1,:), '*-',x,Ratio2(1,:), '*-',x,Ratio3(1,:), '*-'); title('Average Ratio vs. Y distance X = 6
mm')
legend('20 / 40','20 / 60','40 / 60'); xlabel('y (mm)'); ylabel('Intensity');
figure; plot(x,Ratio1(2,:), '*-',x,Ratio2(2,:), '*-',x,Ratio3(2,:), '*-'); title('Average Ratio vs. Y distance X = 31
mm')
legend('20 / 40','20 / 60','40 / 60'); xlabel('y (mm)'); ylabel('Intensity');
figure; plot(x,Ratio1(3,:), '*-',x,Ratio2(3,:), '*-',x,Ratio3(3,:), '*-'); title('Average Ratio vs. Y distance X = 56
mm')
legend('20 / 40','20 / 60','40 / 60'); xlabel('y (mm)'); ylabel('Intensity');

%% Standard Deviation
O_sd=std(O); He_sd=std(He); x2= repmat(x,3,1);
O1sd=O_sd(ind_1); O2sd=O_sd(ind_2); O3sd=O_sd(ind_3);
H1sd=O_sd(ind_1); H2sd=O_sd(ind_2); H3sd=O_sd(ind_3);

figure; errorbar(x2,Ratio1',O1sd); xlabel('y (mm)'); ylabel('Intensity');
legend('x=6','31','56'); title('Average Ratio vs. Y distance Air = 20 psi He = 40');
text(5,.85,'error bars \pm 1 \sigma')
figure; errorbar(x2,Ratio2',O2sd); xlabel('y (mm)'); ylabel('Intensity');
legend('x=6','31','56'); title('Average Ratio vs. Y distance Air = 20 psi He = 60');
text(6,2,'error bars \pm 1 \sigma')
figure; errorbar(x2,Ratio3',O3sd); xlabel('y (mm)'); ylabel('Intensity');
legend('x=6','31','56'); title('Average Ratio vs. Y distance Air = 40 psi He = 60');
text(6,2,'error bars \pm 1 \sigma')

```


IV Characteristic Line Calculation

```
clc; close all; clear;
load ratio115b; load he115b; load he_sum115b;
load ratio120; load he120; load he_sum120;
load ratio127b; load he127b; load he_sum127b;

ratio1=polyfit(he115b,ratio115b,2); ratio3=polyfit(he127b,ratio127b,2);
ratio2=polyfit(he120,ratio120,2); P=polyval(ratio2,0:70);
P2=.4117-[1:9].*.0203; P3=.2290-[1:21].*.0091; P=[P P2 P3];

y115b=interp1(0:100,P,he115b); y120=interp1(0:100,P,he120); y127b=interp1(0:100,P,he127b);
sd_1=std(ratio115b-y115b); sd_2=std(ratio120-y120); sd_3=std(ratio127b-y127b);

figure; plot(he115b,ratio115b,'s', he120,ratio120,'v',he127b, ratio127b,'*'); title('O / He');
hold on; plot(0:100,P,'k'); ratiop=P; xlabel('% Helium'); ylabel('O/He');
legend(['std =' num2str(sd_1)],['std =' num2str(sd_2)],['std =' num2str(sd_3)],'data fit',0);
save ratiop ratiop
```

V Annular Tube Comparison

```

close all; clear; clc; load fluent_exp_mass
load ratio2_02; load x2_02; load ratio2_03; load x2_03; load ratio2_03b; load x2_03b;
load ratio2_06a; load x2_06a; load ratio2_10a; load x2_10a;

t202=ratio2_02([3,:]); t203=ratio2_03([1 2],:); t203b=ratio2_03b([1 4],:);

%% Volumetric percentages based on interpolation from original experiments
load ratiop;
x202=interp1(ratiop,0:100,t202); x203=interp1(ratiop,0:100,t203);
x203b=interp1(ratiop,0:100,t203b); % x206a=interp1(ratiop,0:100,t206a);
figure; plot(x2_02,x202(1,:), '-.', x2_03,x203(1,:), '-.', x2_03b,x203b(1,:), '-.', ...
    x2_03,x203(2,:), '-.', x2_03b,x203b(2,:), '-');
legend('axial = 2.5 mm','3','7','8','10.5',0); xlabel('radial distance (mm)'); ylabel('% He');
title('Annular Tube Diffusion Experiments, % He vs. r')

figure; plot(x1,y1,x2,y2,x4,y4,x6,y6,x8,y8,x10,y10,x12,y12); legend('1','2','4','6','8','10','12')

for i=1:5
    for j=1:2
        mass203(j,i)=(.01*x203(j,i).*08)/(.08*.01*x203(j,i)+1.16*(1-.01*x203(j,i)));
        mass203b(j,i)=(.01*x203b(j,i).*08)/(.08*.01*x203b(j,i)+1.16*(1-.01*x203b(j,i)));
    end
end

figure; plot(x2_03,mass203(1,:), '-.', x2_03,mass203(2,:), '-.', x2_03b,mass203b(2,:), '-.', ...
    x2,y2,x8,y8,x10,y10);
legend('axial = 3 mm','8','10.5','FLUENT 2 mm','FLUENT 8','FLUENT 10',0); xlabel('radial distance (mm)'); ylabel('Mass Fraction He'); title('Annular Tube Diffusion Experiments, Mass Fraction He vs. r'); axis([-2 7.5 0 .7])

%% Normalize using the centerline value
a=1./max(x202,[],2); b=1./max(x203,[],2); c=1./max(x203b,[],2);
N202=x202.*[a]; N203=x203.*[b b b b]; N203b=x203b.*[c c c c];
figure; plot(x2_02,N202(1,:), '-.', x2_03,N203(1,:), '-.', x2_03b,N203b(1,:), '-.', ...
    x2_03,N203(2,:), '-.', x2_03b,N203b(2,:), '-');
legend('2.5','3','7','8','10.5',0); xlabel('radial distance (mm)'); ylabel('Norm (O / He)');
title('Annular Tube Diffusion Experiments, O/He vs. r')

%% Normalize using the centerline value and the radial coordinate when concentration = 1/2
R1=[interp1(N202(1,:),x2_02,.5)];
R2=[interp1(N203(1,:),x2_03,.5); interp1(N203(2,:),x2_03,.5)];
R3=[interp1(N203b(1,:),x2_03b,.5); interp1(N203b(2,:),x2_03b,.5)]; R3(1,1)=3.2158;
new202=x2_02; R202=1./repmat(R1,1,3); N202x=new202.*R202;
new203=repmat(x2_03,2,1); R203=1./repmat(R2,1,5); N203x=new203.*R203;
new203b=repmat(x2_03b,2,1); R203b=1./repmat(R3,1,5); N203bx=new203b.*R203b;
figure; plot(N202x',N202', '-.', N203x',N203', '-.', N203bx',N203b', '-');
legend('2.5','3','7','8','10.5',0); xlabel('r / r_{1/2}'); ylabel('Norm (O / He)');
title('Annular Tube Diffusion Experiments Normalized Curves')

```

VI Wind Tunnel Comparisons

```

clc; clear; close all;
load WT_3_03                                %% Averages March 3rd
O_avg=mean(O); He_avg=mean(He); Ratio=He_avg./O_avg;
ind_1=[1 6 7; 18 13 12; 19 24 25]; %% Air 20 He 40 psi 0; 5; 10 mm
ind_2=[2 5 8; 17 14 11; 20 23 26]; %% Air 20 He 60
ind_3=[3 4 9; 16 15 10; 21 22 27]; %% Air 40 He 60
O_avg1=O_avg(ind_1); O_avg2=O_avg(ind_2); O_avg3=O_avg(ind_3);
He_avg1=He_avg(ind_1); He_avg2=He_avg(ind_2); He_avg3=He_avg(ind_3);
Ratio1=Ratio(ind_1); Ratio2=Ratio(ind_2); Ratio3=Ratio(ind_3);
load WT_3_20                                %% Averages March 20th
O_avgb=mean(O3_20); He_avgb=mean(He3_20); Ratiob=He_avgb./O_avgb;
ind_11=[27 22 21; 10 15 16; 9 4 3]; %% Air 20 He 40 psi 0; 5; 10 mm
ind_21=[26 23 20; 11 14 17; 8 5 2]; %% Air 20 He 60
ind_31=[25 24 19; 12 13 18; 7 6 1]; %% Air 40 He 60
O_avg11=O_avgb(ind_11); O_avg21=O_avgb(ind_21); O_avg31=O_avgb(ind_31);
He_avg11=He_avgb(ind_11); He_avg21=He_avgb(ind_21); He_avg31=He_avgb(ind_31);
Ratio11=Ratiob(ind_11); Ratio21=Ratiob(ind_21); Ratio31=Ratiob(ind_31);
x=[0 5 10];                                %% Ratio Intensity Plots for each case
figure; plot(x,Ratio1(1,:), 's-', x, Ratio11(1,:), 'd-'); title('Air 20 psi He 40 psi X = 6 downstream')
legend('w/o cavity', 'w/cavity'); xlabel('y (mm)'); ylabel('He / O');
figure; plot(x,Ratio2(1,:), 's-', x, Ratio21(1,:), 'd-'); title('Air 20 psi He 60 psi X = 6 downstream')
legend('w/o cavity', 'w/cavity'); xlabel('y (mm)'); ylabel('He / O');
figure; plot(x,Ratio3(1,:), 's-', x, Ratio31(1,:), 'd-'); title('Air 40 psi He 60 psi X = 6 downstream')
legend('w/o cavity', 'w/cavity'); axis([-2 10.2 0 6]); % xlabel('y (mm)'); ylabel('He / O');
figure; plot(x,Ratio1(3,:), 's-', x, Ratio11(3,:), 'd-'); title('Air 20 psi He 40 psi X = 56 downstream')
legend('w/o cavity', 'w/cavity'); xlabel('y (mm)'); ylabel('He / O');
figure; plot(x,Ratio2(3,:), 's-', x, Ratio21(3,:), 'd-'); title('Air 20 psi He 60 psi X = 56 downstream')
legend('w/o cavity', 'w/cavity'); xlabel('y (mm)'); ylabel('He / O');
figure; plot(x,Ratio3(3,:), 's-', x, Ratio31(3,:), 'd-'); title('Air 40 psi He 60 psi X = 56 mm downstream')
legend('w/o cavity', 'w/cavity'); axis([-2 10.2 0 .7]); % xlabel('y (mm)'); ylabel('He / O');

O_sd=std(O); He_sd=std(He);                %% STD plots
O1sd=O_sd(ind_1); O2sd=O_sd(ind_2); O3sd=O_sd(ind_3);
H1sd=O_sd(ind_1); H2sd=O_sd(ind_2); H3sd=O_sd(ind_3);
O_sdb=std(O3_20); He_sdb=std(He3_20);
O1sdb=O_sdb(ind_1); O2sdb=O_sdb(ind_2); O3sdb=O_sdb(ind_3);
H1sdb=O_sdb(ind_1); H2sdb=O_sdb(ind_2); H3sdb=O_sdb(ind_3);

x2= repmat(x,2,1); x3= repmat(x,3,1);     %% Plots using std bars
figure; errorbar(x2,[Ratio3(1,:); Ratio31(1,:)],[O1sd(1,:); O1sdb(1,:)], 'd-'); % xlabel('Y (mm)'); ylabel('He / O');
legend('w/cavity', 'w/o'); % title('He / O Ratio vs. Y Air = 20 psi He = 40'); axis([-2 10.2 0 5.5]);
text(5,2.4,'error bars \pm 1 \sigma'); axis([-3 10.2 0 5.5])
figure; errorbar(x2,[Ratio3(3,:); Ratio31(3,:)],[O3sd(3,:); O3sdb(3,:)], 'd-'); % xlabel('Y (mm)'); ylabel('He / O');
legend('w/cavity', 'w/o'); % title('He / O Ratio vs. Y Air = 20 psi He = 40'); axis([-2 10.2 0 5.5]);
text(1.15,'error bars \pm 1 \sigma'); axis([-3 10.2 0 .6])
figure; errorbar(x3,Ratio2',O2sd,'d-'); xlabel('Y (mm)'); ylabel('He / O');
legend('x=6', '31', '56'); title('He / O Ratio vs. Y Air = 20 psi He = 60'); text(6,2,'error bars \pm 1 \sigma')
figure; errorbar(x3,Ratio3',O3sd,'s-'); xlabel('Y (mm)'); ylabel('He / O');
legend('x=6', '31', '56'); title('He / O vs. Y Air = 40 psi He = 60'); text(6,2,'error bars \pm 1 \sigma')

```